Monthly Notices
of the
ROYAL ASTRONOMICAL SOCIETY

MNRAS **477,** 4543–4564 (2018)
Advance Access publication 2018 March 23

doi:10.1093/mnras/sty734

ADER discontinuous Galerkin schemes for general-relativistic ideal magnetohydrodynamics

F. Fambri,[1⋆] M. Dumbser,[1⋆] S. Köppel,[2,3] L. Rezzolla[2,3⋆] and O. Zanotti[1]

[1] *Laboratory of Applied Mathematics, University of Trento, Via Mesiano 77, I-38123 Trento, Italy*
[2] *Institute for Theoretical Physics, Max-von-Laue-Str 1, D-60438 Frankfurt, Germany*
[3] *Frankfurt Institute for Advanced Studies, Ruth-Moufang-Str 1, D-60438 Frankfurt, Germany*

Accepted 2018 March 12. Received 2018 March 12; in original form 2018 January 9

ABSTRACT

We present a new class of high-order accurate numerical algorithms for solving the equations of general-relativistic ideal magnetohydrodynamics in curved space–times. In this paper, we assume the background space–time to be given and static, i.e. we make use of the Cowling approximation. The governing partial differential equations are solved via a new family of fully discrete and arbitrary high-order accurate path-conservative discontinuous Galerkin (DG) finite-element methods combined with adaptive mesh refinement and time accurate local time-stepping. In order to deal with shock waves and other discontinuities, the high-order DG schemes are supplemented with a novel *a posteriori* subcell finite-volume limiter, which makes the new algorithms as robust as classical second-order total-variation diminishing finite-volume methods at shocks and discontinuities, but also as accurate as unlimited high-order DG schemes in smooth regions of the flow. We show the advantages of this new approach by means of various classical two- and three-dimensional benchmark problems on fixed space–times. Finally, we present a performance and accuracy comparisons between Runge–Kutta DG schemes and ADER high-order finite-volume schemes, showing the higher efficiency of DG schemes.

Key words: black hole physics – MHD – relativistic processes – shock waves – methods: numerical.

1 INTRODUCTION

Electromagnetism plays an important role in many astrophysical processes such as compact objects and binaries consisting of black holes and neutron stars. The general-relativistic magnetohydrodynamics (GRMHD) is a successful theory to describe these systems, combining the fluid description of matter with a simplified theory for electromagnetic fields in the absence of free charge carriers. Similar to general-relativistic hydrodynamics (GRHD), first successful (lower-dimensional) simulations of the GRMHD system date back to the pioneering work of Wilson (1975) more than 40 yr ago (see Font (2008) and Martí & Müller (2015) for recent reviews on progress in GRMHD simulation]. In the past years, several groups started to recast the system of GRMHD equations into a conservative form to make use of conservative Godunov-type finite-volume schemes based on approximate Riemann solvers and high-resolution shock-capturing schemes. Many GRHD and GRMHD codes have been developed over the last decade (for instance, Aninos, Fragile & Salmonson 2005; Baiotti et al. 2005; Duez et al. 2005; Antón et al. 2006; Giacomazzo & Rezzolla 2007; Anderson et al. 2008; Kiuchi et al. 2009; Bucciantini & Del Zanna 2011; Radice & Rezzolla 2012; Dionysopoulou et al. 2013; Radice, Rezzolla & Galeazzi 2014; White, Stone & Gammie 2016; Porth et al. 2017) and applied to various topics in astrophysics. Some codes also evolve the space–time by feeding back the fluid and magnetic energy-momentum tensor in the Einstein field equations, which govern the time evolution of the metric tensor; some codes even incorporate radiation transfer like the one proposed by Takahashi & Umemura (2017), or include the full Maxwell theory in a resistive relativistic MHD formulation (see e.g. Dumbser & Zanotti 2009; Palenzuela et al. 2009; Bucciantini & Zanna 2013; Dionysopoulou et al. 2013; Bugli, Del Zanna & Bucciantini 2014; Aloy & Cordero-Carrión 2016).

In this work, we propose a new family of little dissipative and little dispersive shock capturing schemes for the solution of the GRMHD equations, based on high-order accurate *explicit* discontinuous Galerkin (DG) finite-element schemes on space–time adaptive mesh refinement (AMR) with time-accurate local time-stepping (LTS) and supplemented by a high-order accurate *a posteriori* subcell finite-volume limiter in order to cope with shocks and

⋆ E-mail: francesco.fambri@unitn.it (FF); michael.dumbser@unitn.it (MD); rezzolla@th.physik.uni-frankfurt.de (LR)

discontinuities in the solution. To the best of our knowledge, this family of algorithms has never been applied to the GRMHD equations before.

An important and novel aspect of our approach is the interpretation of the source terms in the GRMHD equations that account for the gravitational field in curved space–times as *non-conservative products*, instead of the usually employed algebraic source terms, since the gravity terms in general relativity are indeed functions of the spatial derivatives of the lapse, the shift vector and the spatial metric tensor. In other words, given a vector of conserved variables $\boldsymbol{Q}$ and the tensor of non-linear conservative fluxes $\boldsymbol{F} = (F^1, F^2, F^3)$, the set of GRMHD equations that are normally written as (Rezzolla & Zanotti 2013)

$$\partial_t \boldsymbol{Q} + \nabla \cdot \boldsymbol{F}(\boldsymbol{Q}) = \boldsymbol{\mathcal{S}}(\boldsymbol{Q}), \tag{1}$$

where $\boldsymbol{\mathcal{S}}$ is a generic source vector can, in our framework, be rewritten as

$$\partial_t \boldsymbol{Q} + \nabla \cdot \boldsymbol{F}(\boldsymbol{Q}) + \boldsymbol{\mathcal{B}}(\boldsymbol{Q}) \cdot \nabla \boldsymbol{Q} = 0, \tag{2}$$

or in quasi-linear form,

$$\partial_t \boldsymbol{Q} + \boldsymbol{\mathcal{A}}(\boldsymbol{Q}) \cdot \nabla \boldsymbol{Q} = 0, \tag{3}$$

with the system matrix $\boldsymbol{\mathcal{A}}(\boldsymbol{Q}) := \partial \boldsymbol{F}/\partial \boldsymbol{Q} + \boldsymbol{\mathcal{B}}(\boldsymbol{Q})$. Above, and throughout the paper, the nabla operator without subscript is simply defined as $\nabla = (\partial_x, \partial_y, \partial_z)$, and thus does not indicate a covariant derivative. Here, $\boldsymbol{\mathcal{B}} = (\boldsymbol{\mathcal{B}}_1, \boldsymbol{\mathcal{B}}_2, \boldsymbol{\mathcal{B}}_3)$ is the matrix of the non-conservative product $\boldsymbol{\mathcal{B}}(\boldsymbol{Q}) \cdot \nabla \boldsymbol{Q} := \boldsymbol{\mathcal{B}}_1 \partial_x \boldsymbol{Q} + \boldsymbol{\mathcal{B}}_2 \partial_y \boldsymbol{Q} + \boldsymbol{\mathcal{B}}_3 \partial_z \boldsymbol{Q}$. The system (3) is called hyperbolic if the matrix $\boldsymbol{\mathcal{A}} \cdot \boldsymbol{n}$ is diagonalizable for all normal vectors $\boldsymbol{n} \neq 0$ with only real eigenvalues and a complete set of bounded linearly independent eigenvectors. The hyperbolicity of the GRMHD system has been studied in many works (see, for instance, Anile 1990; Komissarov 1999).

This paper deals with the general-relativistic extension of the special relativistic case presented in Zanotti, Fambri & Dumbser (2015). As it has been mentioned above, the background space–time is introduced as a *non-conservative product* in the principal part of the system on the left-hand side and is not treated as an algebraic source term, as it has been conventionally treated all along in the literature so far. The inspiration to use so-called path-conservative schemes for non-conservative products has been taken from successful developments in the context of so-called well-balanced numerical methods Bermúdez & Vázquez (1994) for the solution of the shallow-water equations [see Castro, Gallardo & Parés (2006), Parés (2006), and Castro, Pardo & Toro (2010) for details on path-conservative schemes], where the bottom-slope term (which is the gradient of a known function and accounts for gravity forces in shallow-water models) is discretized as a non-conservative product in the principal part of the system rather than as a classical algebraic source term. In the shallow water context, the family of path-conservative schemes allows to preserve certain stationary equilibrium solutions exactly up to machine precision also on the discrete level, including non-trivial equilibria [see Gaburro, Dumbser & Castro (2017) and Gaburro, Castro & Dumbser (2018) for recent examples]. At this stage, the development of exactly well-balanced numerical methods for the GRMHD equations is still out of scope, but further developments in this direction would definitely deserve attention. We also would like to stress that the use of non-conservative products is *not* related to the ADER-DG scheme itself. It would have been equally possible to compute the metric derivatives analytically and discretize the gravity terms as conventional algebraic source terms, as done in other codes for the GRMHD system.

DG methods belong to the family of finite-element methods that consider the numerical approximation of a weak formulation of the governing system of partial differential equations over a set of non-overlapping elements. The discrete solution space is restricted to the space of piecewise polynomials of maximum degree $N \geq 0$ and the degrees of freedom (i.e. the expansion coefficients) of the chosen polynomial basis are directly evolved in time. Finite-element methods are known also under the name of variational-difference or projection difference [see the original formulations by Ritz (1909) and Galerkin (1915)]. In particular, in the DG formulation the numerical solution is allowed to be discontinuous at element interfaces [see Reed & Hill (1973) for the integration of the neutron transport equation]. It has taken nearly two decades for the DG methods to be extended to general non-linear hyperbolic systems, thanks to the ground-breaking works of Cockburn, Lin & Shu (1989), Cockburn, How & Shu (1990) and Cockburn & Shu (1998b); see also Cockburn, Karniadakis & Shu (2000), Cockburn & Shu (2001), and Shu (2016) for a review.

In the last 20 yr, DG methods became increasingly popular mainly because of four attractive properties: (i) non-linear L_2 stability has been proven for general non-linear scalar conservation laws by Jiang & Shu (1994); (ii) arbitrary high order of accuracy can be easily achieved for smooth solutions by simply increasing the polynomial degree N of the chosen basis functions; (iii) high parallel scalability makes DG methods better suited for large-scale simulations even on general unstructured meshes when compared with high-order finite-difference or finite-volume methods; and (iv) high-order DG methods are only little dissipative and little dispersive, even when compared with high-order finite-volume and finite-difference schemes and are thus essential for accurate long-term simulations. The main drawback that afflicts explicit DG schemes is the rather severe CFL stability condition that constrains the time-step of the simulations to scale with approximately $h/(2N + 1)$ for hyperbolic partial differential equations, where N is the degree of the nodal polynomial basis used within the element and h is the characteristic size of one DG element (not the distance between the individual nodal degrees of freedom). A way to alleviate the severe CFL time-step restriction is the use of efficient semi-implicit DG schemes, as those proposed, for instance, by Tavelli & Dumbser (2016) and Fambri & Dumbser (2016).

DG methods have attracted the interest of the computational-astrophysics community only over the last few years. In particular, the first DG-based method for GRHD has been developed by Radice & Rezzolla (2011), but it was limited to spherically symmetric space–times. The first three-dimensional (3D) implementation of a DG method for relativistic flows on curved but fixed background space–times has been recently presented by Bugner et al. (2016), but without considering the magnetic field interaction. Very recently, Miller & Schnetter (2017) formulated an operator-based DG method for the solution of the Einstein field equations, while in Dumbser et al. (2018), a high-order DG scheme for the solution of a first-order reduction of the conformal and covariant formulation (CCZ4; Alic et al. 2012) of the Z4 system of the Einstein equations has been proposed. Also rather recently, Kidder et al. (2017) provided a DG implementation within a task-based parallelism model for GRMHD, while Anninos et al. (2017) presented also a DG code with hp-refinement, and both of them complemented the high resolution of the purely spatial polynomials basis with multistep high-order time integrator, e.g. Adams-Bashforth (AB3) or Runge–Kutta (RK) schemes. Indeed, total-variation diminishing (TVD) RK methods are typically used in order to reach a stable high-order time discretization of DG schemes, i.e.

applying the method of lines (MOL) technique that leads to the so-called family of RK-DG schemes.

On the other hand, the time discretization proposed in this paper is different and is named ADER technique. The particular feature of the ADER approach introduced by Toro and Titarev in the finite-volume context (Titarev & Toro 2002, 2005; Toro & Titarev 2006) is that it leads to arbitrary high-order accurate fully discrete one-step schemes in space and time. ADER schemes have already been applied to the equations of relativistic MHD, both in the ideal case (see Dumbser et al. 2008b; Zanotti & Dumbser 2015; Zanotti et al. 2015b) and in the resistive case (see Dumbser & Zanotti 2009) and to other non-linear systems of partial differential equations (see Zanotti et al. 2015; Fambri, Dumbser & Zanotti 2017). Moreover, the ADER strategy adopted in this paper, which goes back to Dumbser, Enaux & Toro (2008a), applies to general systems of balance laws with conservative fluxes, non-conservative products and stiff or non-stiff algebraic source terms. In particular, it is based on a local space–time discontinuous Galerkin (LSTDG) predictor step, which solves a local Cauchy problem in the small, based on a weak formulation of the partial differential equations in space–time.

Although DG methods are proven to be non-linearly L_2 stable, whenever steep gradients or discontinuities appear in the solution, the use of an unlimited high-order DG scheme inevitably leads to spurious oscillations known as Gibbs phenomenon. In order to cope with this problem, several attempts have been made, e.g. artificial viscosity (Hartmann & Houston 2002; Persson & Peraire 2006; Cesenek et al. 2013), filtering (Radice & Rezzolla 2011), hybridisation with finite-volume/finite-difference schemes for the selected 'troubled cells' adopting some sort of high-order slope-limiting procedures (Cockburn & Shu 1998a; Qiu & Shu 2004, 2005; Balsara et al. 2007; Krivodonova 2007; Luo, Baum & Löhner 2007; Zhu et al. 2008, 2013). Here, we employ to the so-called *a posteriori* finite-volume subcell limiter (SCL) technique recently proposed by Dumbser et al. (2014b), which is based on the so-called multidimensional optimal order detection (MOOD) of Clain, Diot & Loubère (2011) and Diot, Clain & Loubère (2012). The main advantage of this approach is that the high-resolution properties of unlimited DG methods are preserved thanks to the introduction of a subgrid level, which is used *a posteriori* for integrating the partial differential equations in troubled cells by means of a more robust high-order accurate finite-volume scheme [for completeness, see also the work of Casoni et al. (2013), Sonntag & Munz (2014), Sonntag & Munz (2017), Fechter & Munz (2015), and Meister & Ortleb (2016) for alternative subcell DG limiters]. The presented SCL has been applied to several systems of non-linear partial differential equations with promising results in the work of Zanotti et al. (2015 and 2015b) and Fambri et al. (2017).

The paper is organized as follows. In Section 2, we describe the system of governing partial differential equations; in Section 3, we describe the ADER-DG scheme with the finite-volume SCL and the AMR technique. Section 4 presents the testbeds both in special and general relativity that the scheme has passed. In Section 5, we present strong MPI scaling results up to 16 000 MPI ranks and performance and accuracy comparisons between RK-DG schemes and ADER-WENO finite-volume schemes. Finally, Section 6 contains a summary of the results and an outlook to future work. Finally, Section 6 contains a summary of the results and an outlook to future work.

Hereafter, Latin indexes run from 1 to 3, while Greek indexes run from 0 to 3. The zeroth components refer to the time-like coordinate of the corresponding tensor or vector and the signature of the metric tensor is assumed to be $(-,+,+,+)$ throughout the text. We use the Einstein summation convention over repeated indexes. Wherever not specified, the index correspondence $(V^0, V^1, V^2, V^3) = (V^t, V^x, V^y, V^z)$ is adopted. Moreover, bold symbols are used to indicate three-vectors (or tensors). We use units with speed of light $c = 1$ and gravitational constant $G = 1$.

2 MATHEMATICAL FORMULATION AND PHYSICAL ASSUMPTIONS

The governing equations of an (ideal) fluid coupled to an electromagnetic field and described in a curved space–time are given by the GRMHD equations. Following the derivation and formalism developed by Del Zanna et al. (2007), the covariant Euler–Maxwell system reads

$$\nabla_\mu(\rho u^\mu) = 0, \qquad \nabla_\mu T^{\mu\nu} = 0, \qquad \nabla_\mu {}^*F^{\mu\nu} = 0, \tag{4}$$

and contains the conservation of the energy momentum tensor $T^{\mu\nu}$, as well as the homogeneous Faraday law, with ∇_μ being the covariant derivative operator.

Since in most astrophysical phenomena the electrical conductivity of the plasma is very high, the ideal-MHD approximation (where the electrical conductivity is actually assumed to be divergent) is a reasonable one. In this case, the electrical field is completely determined by the fluid velocity and the magnetic field,

$$\boldsymbol{E} = -\boldsymbol{v} \times \boldsymbol{B}, \tag{5}$$

that is, the magnetic flux $\phi_B = \boldsymbol{B} \cdot \boldsymbol{S}$ over any surface S is conserved

$$\oint_{\partial S} (\boldsymbol{E} + \boldsymbol{v} \times \boldsymbol{B}) \cdot \mathrm{d}\boldsymbol{\ell} = -\frac{\mathrm{d}\phi_B}{\mathrm{d}t} = 0, \tag{6}$$

and is advected with the fluid movement. The magnetic contribution to the hydrodynamic equations, i.e. the MHD equations, is then just a conservation equation for the magnetic field, which we will describe in the next sections.

2.1 The 3 + 1 split of space–time

The 3 + 1 decomposition of space–time is the most widely used framework to prepare general-relativistic theories such as the GRMHD for numerical discretization. The four-dimensional space–time manifold is decomposed into 3D space-like hypersurfaces that are parametrized by a time coordinate t and described by the 3D objects (Thorne & Macdonald 1982; Baumgarte & Shapiro 2003; Rezzolla & Zanotti 2013): the lapse function α, the spatial metric tensor $\boldsymbol{\gamma}$, the shift vector $\boldsymbol{\beta}$, and the extrinsic curvature tensor $\boldsymbol{K}$.

The (smooth) foliation or slicing Σ_t defines a time-like normal vector to the three-hypersurface

$$n_\mu = -\alpha \nabla_\mu t, \quad n_\mu = (-\alpha, 0_i), \quad n^\mu = (1/\alpha, -\beta^i/\alpha), \tag{7}$$

which is the future-oriented unit ($n_\mu n^\mu = -1$) vector and can be regarded as the four-velocity of the Eulerian observer, i.e. at rest in the 3D hypersurface Σ_t.

Any four vector V^μ (or tensor) can be split into its temporal and spatial components, respectively

$$-\boldsymbol{n} \cdot \boldsymbol{V} = -n_\mu V^\mu, \tag{8}$$

$$\boldsymbol{\gamma} \cdot \boldsymbol{V} = \left(g^\mu_\nu + n^\mu n_\nu\right) V^\nu, \tag{9}$$

where the relation between the purely spatial (3D) metric tensor γ_{ij} and the spatial-projection operator $\boldsymbol{\gamma}$ is given by

$$\gamma_{\mu\nu} := g_{\mu\nu} + n_\mu n_\nu, \qquad \gamma^\mu_\nu := g^\mu_\nu + n^\mu n_\nu, \tag{10}$$

with the obvious property that $\boldsymbol{\gamma} \cdot \boldsymbol{n} = 0$. In this formalism, the spatial metric γ_{ij} is used for lowering/raising indexes of purely spatial vectors (or tensors).

Given a coordinate system $x^\mu = (t, x^i)$, where $\{x^i\}_{i=1,2,3}$ (or $\boldsymbol{x}$) are the spatial coordinates, the line element on the foliation Σ_t can then be expressed by the $3+1$ form of the metric, i.e.

$$\mathrm{d}s^2 = -\alpha^2 \,\mathrm{d}t^2 + \gamma_{ij} \left(\mathrm{d}x^i + \beta^i \mathrm{d}t\right) \left(\mathrm{d}x^j + \beta^j \mathrm{d}t\right). \tag{11}$$

2.2 The GRMHD system

In order to write the system of the GRMHD equations in the $3+1$ decomposition of the space–time, we define the vector[1] $\boldsymbol{V}$ of the 19 primitive variables as

$$\boldsymbol{V} := \left(\rho, v_j, p, B^j, \Phi, \alpha, \beta^j, \tilde{\gamma}_m\right), \quad j = 1,2,3;\ m = 1,\ldots,6 \tag{12}$$

where ρ is the rest-mass density in the frame comoving with the fluid, $\boldsymbol{v}$ is the three-velocity vector, p is the fluid pressure, $\boldsymbol{B}$ is the magnetic field vector in the comoving frame, Φ is an artificial scalar introduced to ensure the divergence-free constraint of the magnetic field at the discrete level via the hyperbolic divergence-cleaning approach (Dedner et al. 2002), α is the lapse function, $\boldsymbol{\beta}$ is the shift vector, and $\boldsymbol{\gamma}$ is a vector whose components represent the six independent components of the three (spatial) metric $\boldsymbol{\gamma}$, i.e.

$$\tilde{\boldsymbol{\gamma}} = (\gamma_{11}, \gamma_{12}, \gamma_{13}, \gamma_{22}, \gamma_{23}, \gamma_{33}). \tag{13}$$

The corresponding state vector $\boldsymbol{Q}$ of conserved variables is defined as

$$\boldsymbol{Q} := \left(\sqrt{\gamma} D, \sqrt{\gamma} S_j, \sqrt{\gamma}\tau, \sqrt{\gamma} B^j, \Phi, \alpha, \beta^j, \tilde{\gamma}_m\right). \tag{14}$$

Note that while ρ can be seen as the rest-mass density of the fluid evaluated by the Lagrangian comoving observer with four-velocity u^μ, D, and v^μ are the rest-mass density and the velocity as measured by the Eulerian observer. As such, v^μ is a purely spatial vector ($n_\mu v^\mu = 0$) and its norm is the one appearing in the definition of the Lorentz factor W. Finally, the symbol γ denotes instead the determinant of $\boldsymbol{\gamma}$, i.e. $\gamma = \det(\gamma_{ij})$.

Also associated with the Eulerian frame is the (Eulerian) three-momentum density vector S_j, which is related to the Lagrangian velocity u^μ through the following identities:

$$\begin{aligned} u^\mu &= W\left(n^\mu + v^\mu\right), \quad u_\mu u^\mu = -1; \\ W &:= -n_\mu u^\mu = \alpha u^t = (1 - v_i v^i)^{-1/2} = (1 - v^2)^{-1/2}, \\ \boldsymbol{\gamma} \cdot \boldsymbol{u} &= (g^\mu_\nu + n^\mu n_\nu) u^\nu = W v^\mu, \quad v^i = u^i / W + \beta^i / \alpha. \end{aligned}$$

The conserved variables $\boldsymbol{Q}(\boldsymbol{V})$ can be easily expressed in terms of the primitive variables via

$$D := \rho W, \tag{15}$$

$$\boldsymbol{S} := \rho h W^2 \boldsymbol{v} + \boldsymbol{E} \times \boldsymbol{B}, \tag{16}$$

$$U := \rho h W^2 - p + \frac{1}{2}(E^2 + B^2), \tag{17}$$

$$\tau := U - D. \tag{18}$$

[1] Obviously, the state vector is not a physical vector but just an ordered collection of physical degrees of freedom (scalar, vector, and tensor fields). One should refer to this object as a tuple instead.

Here, U is the conserved energy density and τ is the corresponding quantity without the rest-mass energy density, $h = 1 + \epsilon + p/\rho$ is the specific enthalpy, and ϵ is the specific internal energy (Rezzolla & Zanotti 2013).

The electric field in the Eulerian frame is indicated as $\boldsymbol{E}$ and in the ideal-MHD limit (i.e. for diverging electrical conductivities) it is determined by the simple Ohm law (5), i.e. $E_i = -\tilde{\epsilon}_{ijk} v^j B^k$. The cross product is given by the spatial three-Levi-Civita tensor density $\tilde{\epsilon}$

$$\tilde{\epsilon}^{ijk} = \gamma^{-\frac{1}{2}}[ijk], \qquad \tilde{\epsilon}_{ijk} = \gamma^{\frac{1}{2}}[ijk]$$

$$[ijk] = \begin{cases} 1 \text{ for even permutations of } (1,2,3), \\ -1 \text{ for odd permutations}, \\ 0 \text{ otherwise}. \end{cases}$$

The (covariant) Pointing vector $\boldsymbol{E} \times \boldsymbol{B}$ in the momentum density (16) can be written as

$$\begin{aligned} \boldsymbol{E} \times \boldsymbol{B} &= \{\tilde{\epsilon}_{ijk} E^j B^k\} = \{-\tilde{\epsilon}_{ijk} \tilde{\epsilon}^{jmn} v_m B_n B^k\} \\ &= \{v_i \left(B_k B^k\right) - B_i \left(v_k B^k\right)\} = \boldsymbol{v} B^2 - \boldsymbol{B}(\boldsymbol{v} \cdot \boldsymbol{B}). \end{aligned}$$

Given all these definitions, the system of partial differential equations for ideal GRMHD can be written in the very compact nonconservative homogeneous form (2), where the conservative fluxes $\boldsymbol{F}$ and the non-conservative product $\boldsymbol{\mathcal{B}}(\boldsymbol{Q}) \cdot \nabla \boldsymbol{Q}$ are given by

$$\boldsymbol{F} := \gamma^{\frac{1}{2}} \begin{pmatrix} \alpha v^i D - \beta^i D \\ \alpha T^i_j - \beta^i S_j \\ \alpha \left(S^i - v^i D\right) - \beta^i \tau \\ \left(\alpha v^i - \beta^i\right) B^j - \left(\alpha v^j - \beta^j\right) B^i \\ 0 \\ 0 \\ 0 \\ 0 \end{pmatrix}, \tag{19}$$

$$\boldsymbol{\mathcal{B}}(\boldsymbol{Q}) \cdot \nabla \boldsymbol{Q} := \begin{pmatrix} 0 \\ \gamma^{\frac{1}{2}} \left(U \partial_j \alpha - \frac{1}{2} \alpha T^{ik} \partial_j \gamma_{ik} - S_i \partial_j \beta^i\right) \\ \gamma^{\frac{1}{2}} \left(S^j \partial_j \alpha - \frac{1}{2} T^{ik} \beta^j \partial_j \gamma_{ik} - T^j_i \partial_j \beta^i\right) \\ -\beta^j \partial_i \left(\gamma^{\frac{1}{2}} B^i\right) + \alpha \gamma^{\frac{1}{2}} \gamma^{ji} \partial_i \Phi \\ \gamma^{-\frac{1}{2}} \alpha c_h^2 \partial_j \left(\gamma^{\frac{1}{2}} B^j\right) - \beta^j \partial_j \Phi \\ 0 \\ 0 \\ 0 \end{pmatrix}, \tag{20}$$

and where T^{ij} denotes the spatial stress-energy tensor

$$\begin{aligned} T^{ij} &= \rho h W^2 v^i v^j - E^i E^j - B^i B^j + \left[p + \frac{1}{2}\left(E^2 + B^2\right)\right] \gamma^{ij} \\ &= S^i v^j + p_{\mathrm{tot}} \gamma^{ij} - \frac{B^i B^j}{W^2} - (B_k v^k) v^i B^j, \end{aligned} \tag{21}$$

with the total pressure comprising both the fluid and the magnetic pressure, i.e.

$$p_{\mathrm{tot}} = p + p_{\mathrm{mag}} = p + \frac{1}{2}[B^2/W^2 + (B \cdot v)^2]. \tag{22}$$

Since we are here interested in static space–times (Cowling approximation), the system of equations does not contain explicitly the extrinsic-curvature tensor $\boldsymbol{K}$, which can be expressed simply in

terms of metric functions (Misner, Thorne & Wheeler 1973; York 1979; Gourgoulhon 2012):

$$\alpha T^{ij} K_{ij} := \frac{1}{2} T^{ik} \beta^j \partial_j \gamma_{ik} + S^j{}_i \partial_j \beta^i. \tag{23}$$

As mentioned above, the divergence-free constraint of the magnetic field is here taken into account at the discrete level through the so-called hyperbolic Generalized Lagrangian Multiplier (GLM) approach (and also known as 'divergence-cleaning') proposed by Dedner et al. (2002), i.e. by augmenting the GRMHD system with an additional auxiliary equation for an artificial scalar field Φ, in order to propagate away numerical errors in the divergence-free constraint of the magnetic field

$$\partial_i \left(\sqrt{\gamma} B^i \right) = 0. \tag{24}$$

In order to achieve a more efficient divergence cleaning, we also allow the characteristic velocity of the divergence cleaning c_h to be larger than the speed of light, i.e. $c_h \geq 1$ in (19). Typical values for the cleaning speeds are chosen in the range $c_h \in [1, 2]$.

2.3 Equation of state, primitive recovery, characteristic speeds

For the closure of the GRMHD equations, an equation of state $p = p(\rho, \epsilon)$ has to be chosen. With the aim of simplicity, we here consider the ideal-fluid (or 'Gamma-law') equation of state (Section 4)

$$p = \rho\epsilon(\Gamma - 1), \tag{25}$$

where Γ is the polytropic index. In the same spirit, for the recovery of primitive variables $\boldsymbol{V}(\boldsymbol{Q})$, we employ a standard approach corresponding to the third option reported in Section 3.2 of Del Zanna et al. (2007); possible alternatives for performing the inversion of system (16) are discussed by Noble et al. (2006).

For the characteristic wave speeds in GRMHD, we usually employ the standard magnetosonic approximation for the wave speeds (as in Gammie, McKinney & Tóth 2003), but accounting also for the possibility $c_h > 1$. Note that this choice of eigenvalues corresponds to the standard choice when $c_h = 1$ and is also valid in the GRHD limit.

3 NUMERICAL METHODS

3.1 Ader DG schemes

As mentioned in the Introduction section, the numerical scheme that we adopt is the ADER DG scheme supplemented with an *a posteriori* finite-volume SCL approach with AMR, presented in the series of papers Zanotti et al. (2015 and 2015b) and Fambri et al. (2017) in the context of the Euler equations of compressible gas dynamics, ideal MHD, special relativistic RMHD, but also compressible Navier–Stokes and viscous and resistive MHD equations. A brief overview of the numerics is given in the following.

After choosing a mesh partition $\Omega_h = \{\Omega_i\}$, which is Cartesian and space–time adaptive through a *cell-by-cell* approach (see Khokhlov 1998), with the property

$$\Omega = \bigcup_{i=1,\ldots N_E} \Omega_i, \qquad \bigcup_{i\neq j;\ i,j=1,\ldots N_E} \Omega_i^\circ \cap \Omega_j^\circ = \varnothing \tag{26}$$

with Ω being the computational domain, N_E the total number of spatial elements, and '$\circ$' denoting the interior operator. The weak formulation of the governing equations (2) is then written in the form

$$\int_{t^n}^{t^{n+1}} \int_{\Omega_i} \phi_k \left(\partial_t \boldsymbol{Q} + \nabla \cdot \boldsymbol{F}(\boldsymbol{Q}) + \boldsymbol{\mathcal{B}}(\boldsymbol{Q}) \cdot \nabla \boldsymbol{Q} \right) \mathrm{d}\boldsymbol{x}\, \mathrm{d}t = 0, \tag{27}$$

where $\phi_k \in \mathcal{U}_h^N$ is a generic basis element for the vector space $\mathcal{U}_h^N$ of piecewise polynomials of maximum degree $N \geq 0$ defined over Ω and which are allowed to be discontinuous across the element interfaces $\partial\Omega_i$. In this work, the set of basis and test functions $\{\phi_k\}$ has been chosen as the set of Lagrange interpolation polynomials of maximum degree N over Ω_i with the property

$$\phi_k(\boldsymbol{x}^m_{\mathrm{GL},i}) = \begin{cases} 1 & \text{if } k = m; \\ 0 & \text{otherwise;} \end{cases} \qquad k, m = 1, \ldots, (N+1)^{\mathrm{d}} \tag{28}$$

with $\{\boldsymbol{x}^m_{\mathrm{GL},i}\}$ being the set of the Gauss–Legendre (GL) quadrature points in $\Omega_i \subset \mathbb{R}^d$ [see Stroud (1971) for a detailed discussion of multidimensional quadrature]. For this reason, the chosen polynomial basis is said to be a *nodal* basis with respect to the GL quadrature points.

Since the chosen AMR grid is locally Cartesian, the spatial integrals of equation (30) can be evaluated in a *dimension-by-dimension* fashion in x-, y-, and z-directions, and the corresponding nodal test and basis functions are defined after rescaling the domain of integration Ω_i to the unit element $[0, 1]^d$. Therefore, we only need the tensor product of the GL quadrature points in the unit interval [0,1], denoted by $\{\xi^m_{\mathrm{GP}}\}_{m=1,\ldots,N+1}$ in the following. Note that the total number of GL quadrature points $\{\boldsymbol{x}^m_{\mathrm{GP}}\}$ in Ω_i, as well as the total number of basis elements $\{\phi_k\}$, is $(N+1)^d$.

After integration by parts of the flux-divergence term, equation (27) can be rewritten as

$$\begin{aligned} &\int_{t^n}^{t^{n+1}} \int_{\Omega_i} \phi_k\, \partial_t \boldsymbol{Q}\, \mathrm{d}\boldsymbol{x}\, \mathrm{d}t + \int_{t^n}^{t^{n+1}} \int_{\partial\Omega_i} \phi_k\, \boldsymbol{F}(\boldsymbol{Q}) \cdot \boldsymbol{n}\, \mathrm{d}S\, \mathrm{d}t \\ &- \int_{t^n}^{t^{n+1}} \int_{\Omega_i} \nabla\phi_k \cdot \boldsymbol{F}(\boldsymbol{Q})\, \mathrm{d}\boldsymbol{x}\, \mathrm{d}t \\ &+ \int_{t^n}^{t^{n+1}} \int_{\Omega_i} \phi_k\, \boldsymbol{\mathcal{B}}(\boldsymbol{Q}) \cdot \nabla \boldsymbol{Q}\, \mathrm{d}\boldsymbol{x}\, \mathrm{d}t = 0. \end{aligned} \tag{29}$$

After restricting the space of the solutions to the set of piecewise polynomials $\boldsymbol{u}_h(\boldsymbol{x}, t) \in \mathcal{U}_h^N$, i.e.

$$\boldsymbol{u}_h(\boldsymbol{x}, t^n) = \phi_k(\boldsymbol{x})\, \hat{\boldsymbol{u}}_k^n, \quad k = 1, \ldots, (N+1)^d, \quad \boldsymbol{x} \in \Omega_i,$$

the following higher order accurate *path-conservative* ADER-DG scheme is obtained for the so-called degrees of freedom of $\boldsymbol{u}_h$, or expansion coefficients, $\hat{\boldsymbol{u}}_k^n$:

$$\begin{aligned} &\left(\int_{\Omega_i} \phi_k \phi_l\, \mathrm{d}\boldsymbol{x} \right) \left(\hat{\boldsymbol{u}}_l^{n+1} - \hat{\boldsymbol{u}}_l^n \right) \\ &+ \int_{t^n}^{t^{n+1}} \int_{\partial\Omega_i} \phi_k \mathcal{G}\left(\boldsymbol{q}_h^-, \boldsymbol{q}_h^+ \right) \cdot \boldsymbol{n}\, \mathrm{d}S\, \mathrm{d}t \\ &+ \int_{t^n}^{t^{n+1}} \int_{\partial\Omega_i} \phi_k \mathcal{D}\left(\boldsymbol{q}_h^-, \boldsymbol{q}_h^+ \right) \cdot \boldsymbol{n}\, \mathrm{d}S\, \mathrm{d}t \\ &- \int_{t^n}^{t^{n+1}} \int_{\Omega_i} \nabla\phi_k \cdot \boldsymbol{F}(\boldsymbol{q}_h)\, \mathrm{d}\boldsymbol{x}\, \mathrm{d}t \\ &+ \int_{t^n}^{t^{n+1}} \int_{\Omega_i^\circ} \phi_k \boldsymbol{\mathcal{B}}(\boldsymbol{q}_h) \cdot \nabla \boldsymbol{q}_h\, \mathrm{d}\boldsymbol{x}\, \mathrm{d}t = 0, \end{aligned} \tag{30}$$

where an element-local space–time predictor solution $\boldsymbol{q}_h(\boldsymbol{x}, t)$ has been introduced and the details related to its computation are given in the next section.

Due to the discontinuous character of the solution $\boldsymbol{q}_h$ at the element interfaces $\partial\Omega_i$, the surface integral of the fluxes is computed by means of an approximate Riemann solver $\mathcal{G}$ depending on the boundary extrapolated data $\boldsymbol{q}_h^-$ and $\boldsymbol{q}_h^+$ evaluated at the left and right of an element interfaces, respectively. In this paper, we mainly use the simple Rusanov flux (Rusanov 1961)

$$\mathcal{G}\left(\boldsymbol{q}_h^-, \boldsymbol{q}_h^+\right) \cdot \boldsymbol{n} = \frac{1}{2}\left(\boldsymbol{F}(\boldsymbol{q}_h^+) + \boldsymbol{F}(\boldsymbol{q}_h^-)\right) \cdot \boldsymbol{n} - \frac{1}{2} s_{\max}\left(\boldsymbol{q}_h^+ - \boldsymbol{q}_h^-\right) \tag{31}$$

where $s_{\max}$ denotes the maximum signal speed computed in $\boldsymbol{q}_h^-$ and $\boldsymbol{q}_h^+$. Any other monotone numerical flux function could be used equally well; see Toro (2009) for an overview of different Riemann solvers. On the other hand, the jump term of the non-conservative product has been approximated with a so-called path-conservative scheme (Castro et al. 2006; Parés 2006) of the form

$$\begin{aligned}&\mathcal{D}\left(\boldsymbol{q}_h^-, \boldsymbol{q}_h^+\right) \cdot \boldsymbol{n} \\ &= \frac{1}{2}\left(\int_0^1 \boldsymbol{\mathcal{B}}\left(\boldsymbol{\psi}(\boldsymbol{q}_h^-, \boldsymbol{q}_h^+, s)\right) \cdot \boldsymbol{n}\, \mathrm{d}s\right) \cdot \left(\boldsymbol{q}_h^+ - \boldsymbol{q}_h^-\right),\end{aligned} \tag{32}$$

that is based on the theory of Dal Maso, LeFloch & Murat (1995) on hyperbolic partial differential equations with non-conservative products and which must obey the generalized Rankine–Hugoniot or consistency condition

$$\begin{aligned}&\mathcal{D}\left(\boldsymbol{q}_h^-, \boldsymbol{q}_h^+\right) \cdot \boldsymbol{n} - \mathcal{D}\left(\boldsymbol{q}_h^+, \boldsymbol{q}_h^-\right) \cdot \boldsymbol{n} \\ &= \int_0^1 \boldsymbol{\mathcal{B}}\left(\boldsymbol{\psi}(\boldsymbol{q}_h^-, \boldsymbol{q}_h^+, s)\right) \cdot \boldsymbol{n}\, \partial_s \boldsymbol{\psi}\, \mathrm{d}s.\end{aligned} \tag{33}$$

The path $\boldsymbol{\psi} = \boldsymbol{\psi}(\boldsymbol{q}_h^-, \boldsymbol{q}_h^+, s)$ is a Lipschitz continuous function with $0 \le s \le 1$, $\boldsymbol{\psi}(\boldsymbol{q}_h^-, \boldsymbol{q}_h^+, 0) = \boldsymbol{q}_h^-$ and $\boldsymbol{\psi}(\boldsymbol{q}_h^-, \boldsymbol{q}_h^+, 1) = \boldsymbol{q}_h^+$. We here use the simplest possible path, i.e. the straight-line segment path

$$\boldsymbol{\psi} = \boldsymbol{\psi}(\boldsymbol{q}_h^-, \boldsymbol{q}_h^+, s) = \boldsymbol{q}_h^- + s\left(\boldsymbol{q}_h^+ - \boldsymbol{q}_h^-\right), \quad s \in [0, 1], \tag{34}$$

and the line integral in equation (32) is easily evaluated by sufficiently accurate numerical quadrature rules [see Dumbser et al. (2009) and Dumbser & Toro (2011) for details].

Notice that the combination of equation (31) with (32) represents the extension of the Rusanov (or local Lax–Friedrichs) flux to the non-conservative case. Indeed, other more sophisticated schemes may be used with the aim of reducing the numerical dissipation [see e.g. the HLLEM-type version of Dumbser & Balsara (2016), which is an extension of the HLLEM flux of Einfeldt et al. (1991), or the path-conservative Osher schemes forwarded in Dumbser & Toro (2011)].

Note also that the choice made here to interpret the gravity terms as a non-conservative product makes them appear not only in the volume integral in equation (30), but also in the Riemann solver via equation (32). This contribution to the Riemann solver is not present in classical discretizations as purely algebraic source term. However, the main advantage of path-conservative schemes is that they allow at least in principle the construction of well-balanced numerical schemes that are able to preserve particular steady-state solutions of the governing partial differential equations exactly. Although the development of exactly well-balanced schemes for the GRMHD equations is beyond the scope of this work, it represents an interesting extension of the formalism presented here.

As a concluding remark in this section, we note that the ADER-DG scheme (30) is $(N + 1)$th order accurate for smooth solutions. Since the final algorithm is a purely explicit DG scheme, a CFL-type stability condition on the time-step holds in the form

$$\Delta t_{\mathrm{DG}} < \mathrm{CFL}\frac{h_{\min}}{d\,(2N+1)}\frac{1}{|\lambda_{\max}|}, \tag{35}$$

where $h_{\min}$ is the minimum characteristic mesh 'size, d is the number of spatial dimensions, $\lambda_{\max}$ is the maximum signal velocity of the system of partial differential equations, and CFL is a constant coefficient such that $0 < \mathrm{CFL} < 1$. If not stated otherwise, the standard value for the tests presented in this paper is $\mathrm{CFL} = 0.9$. For the results of a numerical von Neumann stability analysis of ADER-DG schemes (see e.g. Dumbser 2005; Qiu et al. 2005; Dumbser et al. 2008b).

3.2 Space–time DG predictor

First introduced in equation (30), the space–time predictor $\boldsymbol{q}_h$ is an *interior* solution of the partial differential equations within each element, based on the following weak formulation of (29) in space–time:

$$\begin{aligned}&\int_{t^n}^{t^{n+1}} \int_{\Omega_i^\circ} \theta_k\, \partial_t \boldsymbol{q}_h\, \mathrm{d}\boldsymbol{x}\, \mathrm{d}t + \int_{t^n}^{t^{n+1}} \int_{\Omega_i^\circ} \theta_k\, \nabla \cdot \boldsymbol{F}(\boldsymbol{q}_h)\, \mathrm{d}\boldsymbol{x}\, \mathrm{d}t \\ &+ \int_{t^n}^{t^{n+1}} \int_{\Omega_i^\circ} \theta_k \boldsymbol{\mathcal{B}}(\boldsymbol{q}_h) \cdot \nabla \boldsymbol{q}_h\, \mathrm{d}\boldsymbol{x}\, \mathrm{d}t = 0,\end{aligned} \tag{36}$$

where the spatial domain of integration has been reduced to only the interior of the space elements Ω_i°, i.e. without integration by parts of the space integrals. As a result, one obtains a system of N_E independent (element-local) equation systems.

Note the introduction here of the new basis set $\{\theta_k\}$ for the vector space $\mathcal{Q}_h^N$ of piecewise space–time polynomials of maximum degree N, and the discrete solution $\boldsymbol{q}_h(\boldsymbol{x}, t)$ is represented in terms of the basis functions θ_k as

$$\boldsymbol{q}_h(\boldsymbol{x}, t) = \theta_k(\boldsymbol{x}, t)\, \hat{\boldsymbol{q}}_k. \tag{37}$$

Also in this case, a nodal basis is used, based on the GL quadrature points referring to the space–time element $\Omega_i \times [t^n, t^{n+1}]$. After integration in time by parts of the first term in equation (36) and after invoking the *causality principle* (upwinding in time), then the following N_E independent systems of $(N + 1)^{(d+1)}$ non-linear equations in the space–time degrees of freedom $\hat{\boldsymbol{q}}_k$ are obtained:

$$\begin{aligned}&\int_{\Omega_i^\circ} \theta_k(\boldsymbol{x}, t^{n+1}) \boldsymbol{q}_h(\boldsymbol{x}, t^{n+1})\, \mathrm{d}\boldsymbol{x} - \int_{\Omega_i^\circ} \theta_k(\boldsymbol{x}, t^n) \boldsymbol{u}_h(\boldsymbol{x}, t^n)\, \mathrm{d}\boldsymbol{x} \\ &- \int_{t^n}^{t^{n+1}} \int_{\Omega_i^\circ} \partial_t \theta_k \boldsymbol{q}_h(\boldsymbol{x}, t)\, \mathrm{d}\boldsymbol{x}\, \mathrm{d}t + \int_{t^n}^{t^{n+1}} \int_{\Omega_i^\circ} \theta_k \nabla \cdot \boldsymbol{F}(\boldsymbol{q}_h)\, \mathrm{d}\boldsymbol{x}\, \mathrm{d}t \\ &+ \int_{t^n}^{t^{n+1}} \int_{\Omega_i^\circ} \theta_k \boldsymbol{\mathcal{B}}(\boldsymbol{q}_h) \cdot \nabla \boldsymbol{q}_h\, \mathrm{d}\boldsymbol{x}\, \mathrm{d}t = 0, \\ &i = 1, 2, \ldots, N_E; \quad k = 1, 2, \ldots, (N+1)^{(d+1)}.\end{aligned} \tag{38}$$

The system of equations (38) can be solved via a simple discrete Picard iteration for each element Ω_i, without needing any communication with neighbour elements (Dumbser et al. 2008b).

We should stress that the choice of an appropriate initial guess $\boldsymbol{q}_h^0(\boldsymbol{x}, t)$ for $\boldsymbol{q}_h(\boldsymbol{x}, t)$ is crucial to obtain a computationally efficient scheme. One can either use an extrapolation of $\boldsymbol{q}_h$ from the previous time interval $[t^{n-1}, t^n]$, as suggested in Zanotti & Dumbser (2016), or a second-order accurate MUSCL-Hancock method, as suggested in Hidalgo & Dumbser (2011). For the initial guess, one can write a Taylor series expansion in time and then simply needs to compute

approximations to the time derivatives of $\boldsymbol{q}_h$ at time t^n, where

$$\begin{aligned}\boldsymbol{\mathcal{L}}(\boldsymbol{u}_h(\boldsymbol{x},t^n)) = &-\nabla\cdot\boldsymbol{F}(\boldsymbol{u}_h(\boldsymbol{x},t^n))\\ &-\boldsymbol{\mathcal{B}}\left(\boldsymbol{u}_h(\boldsymbol{x},t^n)\right)\cdot\nabla\boldsymbol{u}_h(\boldsymbol{x},t^n)\end{aligned} \tag{39}$$

is used as an abbreviation in the following. A second-order accurate MUSCL-type initial guess for for $\boldsymbol{q}_h(\boldsymbol{x},t)$ is given by

$$\boldsymbol{q}_h^0(\boldsymbol{x},t) = \boldsymbol{u}_h(\boldsymbol{x},t^n) + \left(t-t^n\right)\boldsymbol{\mathcal{L}}(\boldsymbol{u}_h(\boldsymbol{x},t^n)), \tag{40}$$

while a third-order accurate initial guess for $\boldsymbol{q}_h(\boldsymbol{x},t)$ reads

$$\boldsymbol{q}_h^0(\boldsymbol{x},t) = \boldsymbol{u}_h(\boldsymbol{x},t^n) + \left(t-t^n\right)\boldsymbol{k}_1 + \frac{1}{2}\left(t-t^n\right)^2\frac{(\boldsymbol{k}_2-\boldsymbol{k}_1)}{\Delta t}, \tag{41}$$

where $\boldsymbol{k}_1 := \boldsymbol{\mathcal{L}}\left(\boldsymbol{u}_h(\boldsymbol{x},t^n)\right)$ and $\boldsymbol{k}_2 := \boldsymbol{\mathcal{L}}\left(\boldsymbol{u}_h(\boldsymbol{x},t^n)+\Delta t\boldsymbol{k}_1\right)$. For an even higher-order accurate initial guess, one can employ the continuous extension Runge–Kutta (CERK) schemes proposed in Owren & Zennaro (1992). For the use of CERK schemes as time integrators of explicit DG schemes, see Gassner et al. (2011). If an initial guess of the order N is chosen, it is sufficient to use *one single* Picard iteration in order to solve equation (38). It is also useful to remark once again that one-step ADER schemes are particularly well suited for AMR with time-accurate LTS and allow a consistent reduction of MPI communications compared to classical RK time-stepping schemes [see Dumbser et al. (2013), Dumbser, Hidalgo & Zanotti (2014a), Zanotti et al. (2015), Zanotti et al. (2015), and Fambri et al. (2017) for details].

Furthermore, in ADER schemes for non-linear hyperbolic PDE, limiters need to be applied only once per time-step, while in RK-based MOL schemes, the limiter needs to be applied in each RK stage again.

For a detailed comparison of RK and ADER finite-volume schemes, see Dumbser, Schwartzkopff & Munz (2006) and Balsara et al. (2013), while RK-DG and Lax-Wendroff DG schemes (the latter are very similar to ADER-DG schemes) have been compared in Qiu et al. (2005), also concerning computational performance. We also show a detailed computational performance comparison between ADER-DG schemes and RK-DG schemes for GRMHD at the end of this paper in Section 5.

3.3 *A posteriori* subcell finite-volume limiter

The ADER-DG scheme (30) is formally of order $N+1$ for smooth solutions; hence, the method must be oscillatory for $N>0$ in the presence of discontinuities, since the scheme is linear in the sense of Godunov (1959), thus inevitably generating spurious oscillations (this is also known as the 'Gibbs phenomenon' in the context of signal analysis). In order to cope with this problem, a special treatment is needed *where*ver and *when*ever the solution is discontinuous, or the gradients in the discrete solution are sufficiently steep. In our specific implementation, this problem is handled as follows: After evaluating the predictor solution $\boldsymbol{q}_h(\boldsymbol{x},t)$ via equation (38), a so-called candidate solution $\boldsymbol{u}_h^*(\boldsymbol{x},t^{n+1})$ is computed through the unlimited one-step ADER-DG scheme (30). Next, the candidate solution $\boldsymbol{u}_h^*(\boldsymbol{x},t^{n+1})$ is checked against mathematical and physical admissibility criteria, which are collectively referred as the relaxed *discrete maximum principle* (DMP). These criteria are the absence of floating point errors (NaNs), the positivity of pressure and density of the fluid, the velocity being lower than the light speed and a possible (successful) conversion from conservative to primitive variables $\boldsymbol{V}=\boldsymbol{V}(\boldsymbol{Q})$ (see Loubère et al. 2014; Zanotti et al. 2015). Typical scenarios that may potentially violate the cited admissibility criteria are the vicinity of steep-gradients or discontinuities, under-resolved flow features, as well as very low pressure and density conditions, e.g. atmospheres around compact objects or vacuum regions.

For the subcell finite-volume limiter, we introduce the notation $\boldsymbol{v}_h(\boldsymbol{x},t^n)=\mathcal{P}\left(\boldsymbol{u}_h(\boldsymbol{x},t^n)\right)$ as the L_2-projection of $\boldsymbol{u}_h$ on to the space of piecewise constant functions on a given subgrid defined within Ω_i, where the individual cells of the subgrid are denoted by $\Omega_{i,s}$ with $\bigcup\Omega_{i,s}=\Omega_i$. Following Dumbser et al. (2014b), Zanotti et al. (2015, 2015b), and Fambri et al. (2017), each element Ω_i is divided into N_s^d equidistant subgrid cells $\Omega_{i,s}$ with $N_s\geq N+1$. If we denote by $\bar{\boldsymbol{v}}_{i,s}^n$ the individual subcell averages within each subcell $\Omega_{i,s}$, then the projection $\mathcal{P}$ reads

$$\bar{\boldsymbol{v}}_{i,s}^n := \frac{1}{|\Omega_{i,s}|}\int_{\Omega_{i,s}}\boldsymbol{u}_h(\boldsymbol{x},t^n)d\boldsymbol{x}. \tag{42}$$

In practice, the relaxed DMP used in this paper reads

$$\min_{\boldsymbol{y}\in\mathcal{V}_i}(\boldsymbol{v}_h(\boldsymbol{y},t^n)) - \delta \leq \boldsymbol{v}_h^*(\boldsymbol{x},t^{n+1}) \leq \max_{\boldsymbol{y}\in\mathcal{V}_i}(\boldsymbol{v}_h(\boldsymbol{y},t^n)) + \delta, \tag{43}$$

where $\mathcal{V}_i$ is the set containing the space element Ω_i and its Voronoi neighbours that share a common node with Ω_i. Here, the parameter δ in (43) is chosen as

$$\delta = \max\left(\delta_0, \epsilon\times\left(\max_{\boldsymbol{y}\in\mathcal{V}_i}(\boldsymbol{u}_h(\boldsymbol{y},t^n)) - \min_{\boldsymbol{y}\in\mathcal{V}_i}(\boldsymbol{u}_h(\boldsymbol{y},t^n))\right)\right), \tag{44}$$

with $\delta_0=10^{-8}$ and $\epsilon=10^{-7}$, which is more restrictive than what used in previous work (Dumbser et al. 2014b; Zanotti et al. 2015).

If the candidate solution $\boldsymbol{u}_h^*$ violates any of the criteria of the relaxed DMP (43), then it is locally rejected and the cell Ω_i is flagged as a troubled cell and a limiter status flag $\tilde{\beta}_i^{n+1}$ is set to $\tilde{\beta}_i^{n+1}=1$; conversely, it is set to $\tilde{\beta}_i^{n+1}=0$ if all admissibility criteria are satisfied in cell Ω_i at time t^{n+1}. For a troubled cell Ω_i, the numerical solution is then recomputed, starting again from the old time level t^n, but using now a more robust numerical scheme than the high-order ADER-DG scheme.

We have here selected as numerical scheme on the subgrid level a second-order accurate MUSCL-Hancock TVD finite-volume scheme with MinMod slope limiter (Toro 2009), mostly because of its proven robustness in the presence of shock waves and low-density atmospheres. For cells that were unlimited at the old time (i.e. $\beta_i^n=0$), it is easy to compute the necessary subcell averages via the projection (42), while for limited cells at time t^n, the subcell averages are already available from the previous time-step. As an alternative, a higher accurate ADER-WENO finite-volume schemes can be used (see Dumbser et al. 2013; Dumbser et al. 2014b), bearing in mind that the WENO approach does not clip local extrema, in contrast to the chosen second-order TVD method. However, for the GRMHD system considered here we have found the subcell TVD limiter to be much more robust than the WENO scheme.

Formally, we can write both the second-order MUSCL-Hancock scheme, as well as a high-order ADER-WENO scheme, as

$$\begin{aligned}\bar{\boldsymbol{v}}_{i,s}^{n+1} - \bar{\boldsymbol{v}}_{i,s}^n &+ \int_{t^n}^{t^{n+1}}\int_{\partial\Omega_{i,s}}\mathcal{G}\left(\boldsymbol{q}_h^-,\boldsymbol{q}_h^+\right)\cdot\boldsymbol{n}\,\mathrm{d}S\,\mathrm{d}t\\ &+\int_{t^n}^{t^{n+1}}\int_{\partial\Omega_{i,s}}\mathcal{D}\left(\boldsymbol{q}_h^-,\boldsymbol{q}_h^+\right)\cdot\boldsymbol{n}\,\mathrm{d}S\,\mathrm{d}t\\ &+\int_{t^n}^{t^{n+1}}\int_{\Omega_{i,s}^\circ}\boldsymbol{\mathcal{B}}(\boldsymbol{q}_h)\cdot\nabla\boldsymbol{q}_h\,\mathrm{d}\boldsymbol{x}\,\mathrm{d}t = 0,\end{aligned} \tag{45}$$

which is very similar to the ADER-DG scheme (45).

High order in space, together with non-oscillatory properties, are achieved in equation (45) via a non-linear reconstruction of piecewise polynomials from the known cell averages $\bar{\boldsymbol{v}}_{i,s}^{n}$ using either a TVD or a WENO reconstruction. Denoting by $\boldsymbol{w}_h(\boldsymbol{x}, t^n)$ the result of this reconstruction, it can then be used to compute the predictor $\boldsymbol{q}_h(\boldsymbol{x}, t)$, either via equation (38), where $\boldsymbol{u}_h(\boldsymbol{x}, t^n)$ is simply replaced by $\boldsymbol{w}_h(\boldsymbol{x}, t^n)$ and the control volume of the space–time integration is replaced by $\Omega_{i,s} \times [t^n, t^{n+1}]$, or via the simple MUSCL-Hancock evolution step to the half-time level [see Toro (2009) for details].

From equation (45), a new piecewise constant solution $\boldsymbol{v}_h(\boldsymbol{x}, t^{n+1})$ given by the cell averages $\bar{\boldsymbol{v}}_{i,s}^{n+1}$ is obtained, from which we can then reconstruct the final, limited DG polynomial as $\boldsymbol{u}_h(\boldsymbol{x}, t^{n+1}) = \mathcal{R}(\boldsymbol{v}_h(\boldsymbol{x}, t^n))$, where $\mathcal{R}$ is the reconstruction operator associated with the projector $\mathcal{P}$, so that $\mathcal{R} \circ \mathcal{P} = \mathcal{I}$, with $\mathcal{I}$ the identity operator [see Dumbser et al. (2014b) for details]. For the subcell finite-volume scheme, a different CFL stability condition applies and takes the form

$$\Delta t_{\mathrm{FV}} < \mathrm{CFL} \frac{h_{\min}}{d\, N_s} \frac{1}{|\lambda_{\max}|}, \tag{46}$$

with $h_{\min}$ the minimum cell size referred to the DG control volumes Ω_i. Choosing $N_s \geq N + 1$ is a natural requirement that allows to reconstruct the of degrees of freedom of $\boldsymbol{u}_h$ from the piecewise constant solution $\boldsymbol{v}_h$ via $\mathcal{R}$. Following Dumbser et al. (2014b), we choose $N_s = 2N + 1$ so that $\Delta t_{\mathrm{FV}} = \Delta t_{\mathrm{DG}}$. This choice allows us to maximize the resolution properties of the chosen subcell finite-volume scheme and to run it at its maximum possible CFL number. For alternative higher order ADER-WENO finite-volume schemes for the relativistic MHD equations with reconstruction in primitive variables, the reader is referred to Balsara & Kim (2016) and Zanotti & Dumbser (2016).

3.4 Adaptive mesh refinement

The ADER-DG algorithms with subcell finite-volume limiter described above has been here implemented on space–time adaptive Cartesian meshes. Detains on our AMR algorithm have been described in Dumbser et al. (2013) and in Zanotti et al. (2015, as well as 2015 b) and Fambri et al. (2017), and we refer the interested reader to these works. The AMR strategy adopted here is named 'cell-by-cell' refinement and consists in providing a space-tree data structure (see Khokhlov 1998; Bungartz et al. 2010; Weinzierl & Mehl 2011; Dumbser et al. 2013, for details), whose 'leaves' correspond to the spatial elements Ω_i used by the numerical scheme described before. The main alternative to a space-tree data structure is the use of so-called *patches* (see Berger & Oliger 1984; Berger & Jameson 1985; Berger & Colella 1989), where a set of independent overlaying Cartesian subgrid domains, or 'patches', is introduced and activated when necessary. In our AMR approach, the numerical solution is checked independently along every single space element for an eventual recursive refining or recoarsening process.

In practice, starting from an initial Cartesian grid of refinement level $\ell = \ell_0 = 0$, which is the basic mesh without refinement, the tree-type infrastructure of finer refinement levels is made accessible. The refinement levels $\ell > 0$ are built according to the so-called refinement factor $\mathcal{R}$ that is the number of smaller space elements per space direction in which a coarser element is broken in a refinement process, or which are merged in a recoarsening stage. Note that choosing a refinement factor $\mathcal{R} = 2$ would generate the well-known 'quadtrees' in two-dimensional (2D) meshes and 'octrees' in 3D meshes. For an arbitrary refinement factor $\mathcal{R}$, general space-trees are obtained (see also Bungartz et al. 2010; Weinzierl & Mehl 2011).

For practical purposes, a finite number of refinement levels is provided, i.e. from the coarser $\ell = \ell_0$ to a finest possible refinement level $\ell = \ell_{\max} \in \mathbb{N}_0^+$. The refinement/recoarsening process is driven by a prescribed refinement-estimator function $\chi = \chi(\boldsymbol{u}_h(\boldsymbol{x}, t^n))$, which is a function of discrete gradients and second derivatives of a scalar *indicator function* φ, and by two thresholds χ^+ and χ^-. Elements are marked for refinement whenever $\chi > \chi^+$ and for recoarsening whenever $\chi < \chi^-$ [for details on the definition of χ, see Löhner (1987), Zanotti et al. (2015), and Fambri et al. (2017)]. In general, the indicator function φ can be chosen to be any mathematical quantity of physical interest that varies in the computational domain and time, e.g. the local rest-mass density, the pressure, or a function of the state variables and of their gradients, e.g. the Lorentz factor, the vorticity, or the limiting-status β_i^n. Hereafter and unless stated otherwise, we have simply used the rest-mass density as indicator function, i.e. $\varphi = \rho$. An alternative choice of χ that deserves investigations in the future would consist in the evaluation of the numerical production of entropy as both error and smoothness indicator [see Puppo & Semplice (2011), Semplice, Coco & Russo (2016), and Cravero & Semplice (2016) for details], but has not yet been used in this paper.

To simplify the AMR algorithm, two neighbour elements are allowed to belong either to the same level ℓ or to an adjacent refinement level $\ell \pm 1$. To each element in the tree, we assign a basic element status which is

$$\sigma_i = \begin{cases} -1, & \text{for the so} - \text{called } \textit{parent cells} \\ 0, & \text{for } \textit{active elements} \\ +1, & \text{for the so} - \text{called } \textit{virtual children} \end{cases} \qquad i = 1, \ldots, N_{\mathrm{tot}}, \tag{47}$$

where N_{tot} is the total number of space elements present in the tree. Note that N_{tot} should be distinguished from the total number of active elements N_E, which are the leaves of the tree that define the Ω_i used in the numerical scheme, and for which $N_{\mathrm{tot}} > N_E$ holds in general. The so-called parent cells ($\sigma_i = -1$) are those tree elements that contain active elements on a higher level and finally a virtual child cell ($\sigma_i = +1$) is a tree element that is contained within an active cell that belongs to a lower and adjacent refinement level $\ell - 1$.

Apart from the storage of flux contributions from neighbour cells within our high-order time-accurate LTS algorithm (Dumbser et al. 2013), virtual cells are also needed for high-order finite-volume schemes to provide the necessary data for polynomial reconstructions (TVD, WENO) on a given refinement level if two adjacent active cells belong to different refinement levels; this is illustrated schematically in Fig. 1. This strategy produces a locally uniform grid around each cell and greatly simplifies reconstruction. Our strategy of generating a locally uniform grid around each cell is very different from the approach based on genuinely multidimensional CWENO reconstructions proposed by Semplice et al. (2016).

The dynamics of the numerical solution on virtual elements is given by standard L_2 projection (for virtual children) or averaging (for parent cells), as depicted in Fig. 2, where the mapping between the chosen solution spaces, piecewise polynomial (unlimited), or piecewise constant (limited), and between two adjacent refinement levels ℓ and $\ell + 1$, is depicted.

Finally, due to the possibility of handling a large range of spatial scales within the same domain, corresponding to very different CFL time restrictions, a time-accurate and fully conservative LTS has been implemented in order to use the smallest admitted

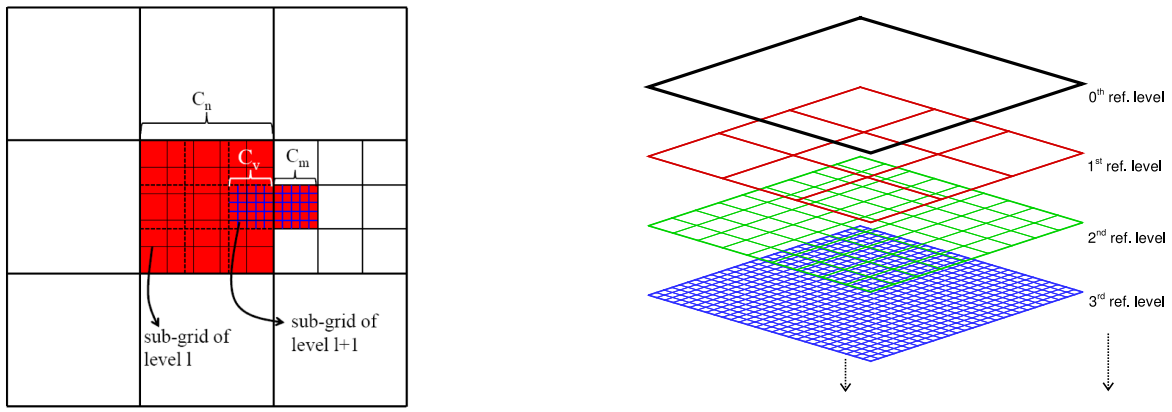

Figure 1. On the left, an example of combination of AMR and DG subcell reconstruction is shown. The limited cells ($\beta = 1$) $\mathcal{C}_n$ and $\mathcal{C}_m$ are highlighted in red. The simplest way for the polynomial reconstruction between $\mathcal{C}_n$ and $\mathcal{C}_m$ elements is (i) project the piecewise constant solution from $\mathcal{C}_n$ to the virtual child-element $\mathcal{C}_v$ (see Fig. 2); (ii) do polynomial reconstruction along the same refinement level, between $\mathcal{C}_v$ and $\mathcal{C}_m$. At the right, the *space-tree* structure of the refinement levels for a single element at the coarsest level ℓ_0 is shown, corresponding to the choice $\mathcal{R} = 3$.

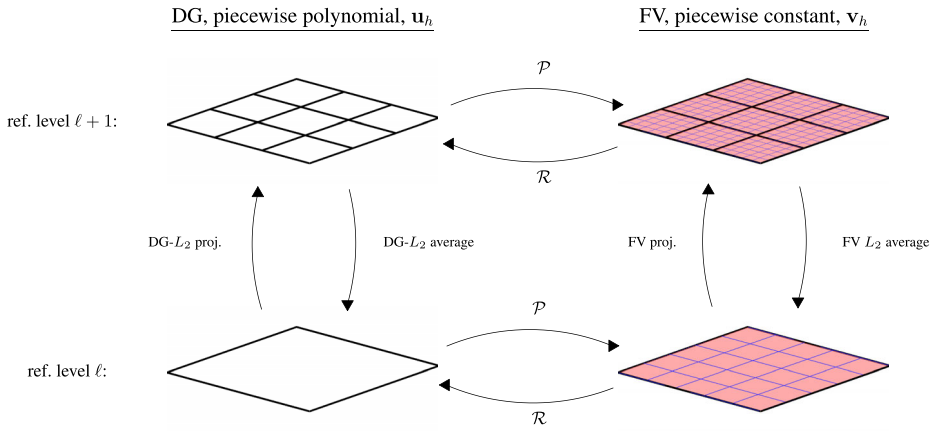

Figure 2. Mapping of the numerical solution between the piecewise polynomials $\boldsymbol{u}_h$ of the DG scheme and the piecewise constant data $\boldsymbol{v}_h$ of the finite-volume scheme as well as between two different AMR levels ℓ and $\ell + 1$.

time-step only where necessary, and a large time-step where it is allowed (see Dumbser et al. 2013). A flow diagram illustrating the main stages of the final algorithm presented in this section can be found in Dumbser et al. (2014b).

4 NUMERICAL VALIDATION

In the following sections, we will present a series of numerical validations of the numerical algorithms introduced so far and characterized by a path-conservative ADER-DG scheme supplemented by an *a posteriori* finite-volume limiter applied to AMR grids. The tests have been performed both in special and in general relativity, employing either two or three spatial dimensions. Furthermore, the validations will be distinguished in 'smooth flows' (Section 4.1), for which we will be able to measure the actual convergence order of the scheme, and 'non-smooth flows' (Sections 4.2 and 4.3), for which we will illustrate the ability of our approach to handle accurately shocks and large gradients.

All of these tests share a number of common properties that we list below and have been employed unless stated otherwise: (i) the adiabatic index has been chosen equal to $\Gamma = 4/3$; (ii) the refinement factor has been chosen as $\mathcal{R} = 3$; (iii) a second-order MUSCL-Hancock TVD finite-volume method with reconstruction in primitive variables on the subgrid-level has been employed as subcell finite-volume limiter for the ADER-DG $\mathbb{P}_N$ method; (iv) the Rusanov (or local Lax–Friedrichs) approximate Riemann solver has been used; and (v) problems in curved space–times have been solved employing Kerr–Schild (KS) coordinates, either spherical or Cartesian.

4.1 Smooth general-relativistic flows

We first test the high order of convergence of our ADER-DG schemes against three different scenarios in curved space–times given, respectively, by (i) the Michel accretion of gas on to a black hole in KS spherical (KSS) coordinates and in 2D; (ii) a stationary non-self-gravitating fluid torus in equilibrium around a black hole, again in 2D; and (iii) the Michel accretion with a radial magnetic field in KS Cartesian (KSC) coordinates and in 3D.

To ensure that the flow is actually smooth, in the following tests we will restrict our computational domain to regions that are fully filled with fluid. In this way, after successively refining the mesh, we evaluate the L_2 and L_∞ error norms at different DG polynomial degrees and mesh resolutions so as to measure the convergence order of our numerical implementation and compare it with the expected mathematical one. Anticipating what will be shown in more detail in

Table 1. L_2 and L_∞ errors and convergence rates for the 2D Michel accretion in spherical KS coordinates for the ADER-DG-$\mathbb{P}_N$ scheme. We report the convergence results for the rest-mass density ρ at $t = 10$ up to $N = 6$, and contrast the results with the expected rate. The domain has been chosen different (enlarged) for the cases $N = 5$ and $N = 6$ in order to keep away the numerical error from the machine limit. Similar results have also been obtained for all other flow variables.

	N_x	$\mathcal{E}_{L_2}$	$\mathcal{E}_{L_\infty}$	L_2	L_∞	Exp.
DG-$\mathbb{P}_1$	10	5.51E−05	9.95E−05	–	–	2
	20	1.26E−05	2.35E−05	2.13	2.08	
	40	3.01E−06	5.70E−06	2.06	2.05	
	80	7.39E−07	1.40E−06	2.03	2.02	
DG-$\mathbb{P}_2$	6	2.53E−05	3.26E−05	–	–	3
	12	3.32E−06	4.46E−06	2.93	2.87	
	18	1.01E−06	1.37E−06	2.93	2.91	
	30	2.26E−07	3.07E−07	2.94	2.93	
DG-$\mathbb{P}_3$	4	3.93E−07	1.11E−06	–	–	4
	6	5.95E−08	1.72E−07	4.65	4.59	
	8	1.77E−08	4.70E−08	4.21	4.51	
	12	3.55E−09	8.05E−09	3.96	4.35	
DG-$\mathbb{P}_4$	2	3.83E−06	5.36E−06	–	–	5
	3	4.10E−07	5.16E−07	5.51	5.77	
	4	9.13E−08	1.23E−07	5.22	4.97	
	5	2.88E−08	4.11E−08	5.18	4.93	
DG-$\mathbb{P}_5$	2	6.33E−08	3.30E−08	–	–	6
	3	4.22E−09	2.36E−09	6.68	6.50	
	4	6.88E−10	3.85E−10	6.31	6.30	
	5	1.70E−10	1.05E−10	6.27	5.83	
DG-$\mathbb{P}_6$	2	1.08E−08	4.67E−09	–	–	7
	3	4.56E−10	2.51E−10	7.81	7.21	
	4	5.38E−11	3.62E−11	7.43	6.72	
	5	1.04E−11	8.11E−12	7.37	6.71	

Table 2. L_2 and L_∞ errors and convergence rates for the 2D torus-interior problem in spherical KS coordinates for the ADER-DG-$\mathbb{P}_N$ scheme. We report the convergence results for the rest-mass density ρ at $t = 10$ up to $N = 4$, and contrast the results with the expected rate. Similar results have also been obtained for all other flow variables.

	N_x	$\mathcal{E}_{L_2}$	$\mathcal{E}_{L_\infty}$	L_2	L_∞	Exp.
DG-$\mathbb{P}_1$	10	5.05E−07	2.67E−06	–	–	2
	20	1.58E−07	9.14E−07	1.68	1.55	
	30	7.52E−08	4.34E−07	1.83	1.84	
	40	4.40E−08	2.50E−07	1.86	1.92	
DG-$\mathbb{P}_2$	10	5.29E−08	1.42E−07	–	–	3
	15	1.81E−08	5.22E−08	2.65	2.47	
	20	8.45E−09	2.35E−08	2.64	2.78	
	30	2.83E−09	7.84E−09	2.70	2.70	
DG-$\mathbb{P}_3$	8	3.65E−09	1.97E−08	–	–	4
	10	1.60E−09	9.77E−09	3.69	3.13	
	15	3.12E−10	2.10E−09	4.04	3.79	
	20	1.08E−10	7.36E−10	3.69	3.64	
DG-$\mathbb{P}_4$	2	1.03E−07	3.60E−07	–	–	5
	3	1.07E−08	3.96E−08	5.57	5.44	
	4	3.30E−09	1.15E−08	4.10	4.29	
	5	1.33E−09	5.85E−09	4.08	3.04	

the following sections, the numerical results confirm the high order of accuracy of the presented numerical scheme. Indeed, using the results shown in Tables 1–3, we can conclude that the ADER-DG $\mathbb{P}_N$ method reaches its design accuracy $N + 1$ in most cases.

Table 3. L_2 and L_∞ errors and convergence rates for the 3D Michel accretion with radial magnetic field in Cartesian KS coordinates for the ADER-DG-$\mathbb{P}_N$ scheme. We report the convergence results for the magnetic field component B^x at $t = 10$ up to $N = 6$, and contrast the results with the expected rate. Similar results have also been obtained for all other flow variables.

	N_x	$\mathcal{E}_{L_2}$	$\mathcal{E}_{L_\infty}$	L_2	L_∞	Exp.
DG-$\mathbb{P}_1$	10	6.588E−04	2.163E−04	–	—	2
	20	1.69E−04	8.258E−05	1.96	1.39	
	30	7.56E−05	4.193E−05	1.99	1.67	
	40	4.26E−05	2.490E−05	2.00	1.81	
DG-$\mathbb{P}_2$	10	3.75E−05	2.39E−05	–	–	3
	15	1.35E−05	7.40E−06	2.53	2.90	
	20	6.62E−06	3.61E−06	2.47	2.49	
	30	2.44E−06	1.35E−06	2.46	2.42	
DG-$\mathbb{P}_3$	8	1.73E−06	1.15E−06	–	–	4
	10	2 6.38E−07	3.72E−07	4.47	5.05	
	15	1.10E−07	6.67E−08	4.35	4.24	
	20	3.25E−08	1.83E−08	4.22	4.50	
DG-$\mathbb{P}_4$	6	4.45E−07	4.17E−07	–	–	5
	8	1.04E−07	9.78E−08	5.05	5.04	
	12	1.35E−08	1.19E−08	5.03	5.19	
	16	3.20E−09	2.58E−09	5.01	5.33	
DG-$\mathbb{P}_5$	4	1.90E−07	3.92E−07	–	–	6
	6	1.32E−08	3.65E−08	6.57	5.85	
	8	2.37E−09	6.29E−09	5.98	6.12	
	10	6.42E−10	1.60E−09	5.85	6.14	
DG-$\mathbb{P}_6$	6	1.26E−06	1.77E−06	–	–	7
	8	1.72E−07	3.96E−07	6.93	5.20	
	10	4.13E−08	1.09E−07	6.39	5.78	
	12	1.34E−08	3.65E−08	6.18	5.99	

For all these convergence tests, since the reference solutions are stationary in time, we used the initial condition as the external state vector in the chosen approximate Riemann solver whenever evaluating the fluxes *only at the boundary interfaces* $\boldsymbol{x} \in \partial\Omega$.

4.1.1 2D Michel accretion on to a Schwarzschild black hole

As a first test of a smooth flow with an analytical solution, we consider the spherical transonic accretion of an isentropic fluid on to a non-rotating black hole is known as Michel solution (Michel 1972). For the sake of completeness, we give the explicit expressions of the lapse, the shift and the spatial metric of a Kerr black hole with mass M and spin a in Cartesian KS coordinates (x, y, z)

$$\alpha = S^{-\frac{1}{2}}, \quad \beta^i = \frac{2H}{S} l_i, \quad H = M\frac{r^3}{r^4 + a^2 z^2}, \quad S = 1 + 2H,$$

$$\gamma_{ij} = \begin{pmatrix} 1 + 2Hl_x^2 & 2Hl_x l_y & 2Hl_x l_z \\ 2Hl_x l_y & 1 + 2Hl_y^2 & 2Hl_y l_z \\ 2Hl_x l_z & 2Hl_y l_z & 1 + 2Hl_z^2 \end{pmatrix}, \tag{48}$$

with

$$l_x := \frac{rx + ay}{r^2 + a^2}, \qquad l_y := \frac{ry - ax}{r^2 + a^2}, \qquad l_z := \frac{z}{r},$$

and

$$r = \sqrt{\frac{x^2 + y^2 + z^2 - a^2}{2} + \sqrt{\left(\frac{x^2 + y^2 + z^2 - a^2}{2}\right)^2 + z^2 a^2}}.$$

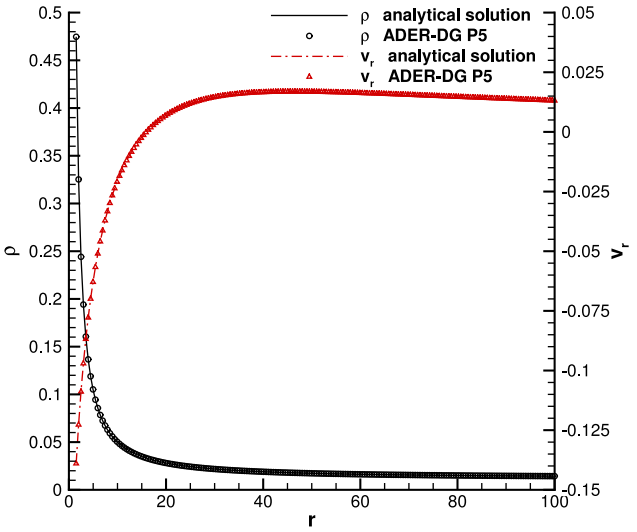

Figure 3. Numerical solution for the 2D Michel accretion test in KSS coordinates obtained with our ADER-DG $\mathbb{P}_5$ at $t = 100$. The numerical solution of density (black) and radial velocity (red) interpolated along 200 points at $\theta = 1.5$ are plotted. The numerical domain is $(r, \theta) \in \Omega = [1.5, 100] \times [0.15, 3.0]$.

Conversely, the Kerr metric in spherical KS coordinates (r, θ, ϕ) is given by Komissarov (2004)

$$\alpha = (1+z)^{-\frac{1}{2}}, \quad \beta^i = \left(\frac{z}{1+z}, 0, 0\right),$$

$$\gamma_{ij} = \begin{pmatrix} 1+z & 0 & -a\sin^2\theta(1+z) \\ 0 & \rho^2 & 0 \\ -a\sin^2\theta(1+z) & 0 & \Sigma\sin^2\theta/\rho^2 \end{pmatrix}, \tag{49}$$

with

$$\rho^2 := r^2 + a^2\cos^2\theta, \qquad z := \frac{2r}{\rho^2},$$

$$\Delta := r^2 + a^2 - 2Mr, \qquad \Sigma = (r^2+a^2)^2 - a^2\Delta\sin^2\theta.$$

After taking the metric (49) with $a = 0$ and defining the values of the free parameters of the problem, i.e. the mass of the black hole $M = 1$, the critical radius $r_c = 8M$, and the critical density $\rho_c M^2 = 1/16$, the Michel solution can be determined analytically (see e.g. Rezzolla & Zanotti 2013).

We have performed this test in spherical KS coordinates with a spatial domain $(r, \theta) \in \Omega = [1.5, 100] \times [0.15, 3.0]$, discretized with a uniform mesh of 200×32 elements and solved with our ADER-DG $\mathbb{P}_5$ scheme. A graphical representation of the numerical results and their comparison with the analytic solution is shown in Fig. 3, while the results of the convergence study are provided in Table 1. Clearly, we can note an excellent agreement between analytical and numerical solution and that the latter converges at the expected and high order.

4.1.2 2D torus interior around a Schwarzschild black hole

Next, we consider the numerical convergence study of a stationary solution of a thick disc (or axisymmetric test-fluid torus) orbiting around a Schwarzschild black hole ($a = 0$) of mass $M = 1$ in 2D spherical KS coordinates. The theory of the equilibrium of these non-self-gravitating fluids in GRHD has been first proposed by Abramowicz, Jaroszynski & Sikora (1978) and Kozlowski, Jaroszynski & Abramowicz (1978), and has been the subject of a vast literature. For completeness, we give in Appendix A a brief description of the set-up of the primitive variables of this test problem, referring the interested reader to Font & Daigne (2002) or to chapter 11 of Rezzolla & Zanotti (2013), and also to Antón et al. (2006) and Del Zanna et al. (2007) for details about a more general configuration of the fluid, depending on the selected values of physical parameters.

The free parameters of the problem have been chosen to be a specific angular momentum of $\ell_0 = 3.8$, a potential gap $\Delta W = -10^{-3}$ (inside and nearly filling its Roche lobe). The polytropic constant and exponent have been chosen equal to $K = 0.0496$ and $\Gamma = 4/3$, respectively.

Also in this case, for a rigorous testing of the convergence order we have simulated only an inner portion of the torus which is fully filled by fluid, namely, the one covered by the coordinate patch $(r, \theta) \in \Omega = [7, 10.5] \times [1.47, 1.67]$. The corresponding measured convergence order after evolving the set of the GRHD equations in spherical KS coordinates are reported in Table 2, once again showing the expected high order of convergence of our ADER-DG scheme. We conclude this test by remarking that torus simulations where the torus is fully contained in the computational domain, which therefore includes also a region set to atmosphere, will be presented in Section 4.3.1.

4.1.3 3D Michel accretion with radial magnetic field

This is the 3D version of the similar test presented in Section 4.1.2, with the addition of one spatial dimension (corresponding to the azimuthal Killing vector) and of a radial magnetic field. Although such a magnetic field is unphysical, since it leads to a non-zero divergence and hence to the presence of a magnetic monopole, it is nevertheless widely used for testing GRMHD codes (see e.g. Etienne, Liu & Shapiro 2010). Here, we use it to test the convergence order of our high-order method by considering also the magnetic component of the set of partial differential equations. In addition, to stress-test our numerical infrastructure, we have employed for this test 3D Cartesian KS coordinates, so that the magnetic field lines are not aligned with any of the coordinate axis.

The chosen contravariant components of the radial magnetic field takes the form

$$B^i(\boldsymbol{x}, t) = \gamma^{-\frac{1}{2}} M^2 B_0 \frac{x^i}{r^2}, \qquad B_0 = \frac{2.688}{M}\left(\frac{b^2}{\rho}\right)^{\frac{1}{2}}_{\rm hor}, \tag{50}$$

where the black hole mass is again set to $M = 1$ and b^μ is the magnetic field measured by the Lagrangian observer comoving with the fluid, i.e.

$$b^\mu := \frac{\left(\delta^\mu_\nu + u^\mu u_\nu\right) B^\nu}{-n_\nu u^\nu}. \tag{51}$$

The spatial domain is in this case given by $(x, y, z) \in \Omega = [-5, +5]^3$ and is partitioned with a uniform mesh of 30^3 elements, where we have employed a very simple cubic excision to avoid the singularities at the coordinates' origin location of the black hole as shown in the left-hand panel of Fig. 4. At the excision boundary, we impose the exact solution of the problem as boundary condition in all variables.

After adopting a ratio $(b^2/\rho)_{\rm hor} = 4$ at the horizon, the results of the convergence study are presented in Table 3, while graphical

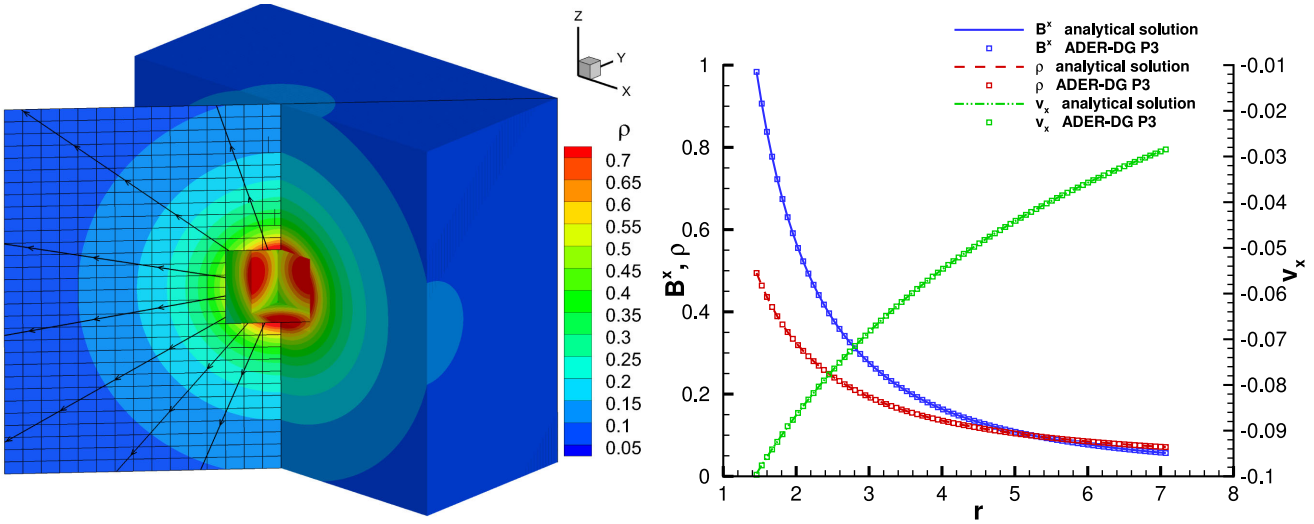

Figure 4. Numerical solution for the 3D Michel accretion test with radial magnetic field in KSC coordinates obtained with our ADER-DG $\mathbb{P}_3$ at $t = 20$. Left-hand panel: 3D visualization of the numerical solution and mesh: the space elements at $y < 0$ are artificially blanked (not visible), at $y > 0$ are coloured by the rest-mass density. Moreover, the computed density is shown also along the 2D cut-plane $y = x \leq 0$ together with the stream-traces of the magnetic field. Right-hand panel: numerical solution interpolated along 200 points at $z = 0$ and $y = x$ for the rest-mass density (red), the x-component of the velocity (green) and magnetic field (blue) vectors are plotted next to the analytical solution. The numerical domain is $\boldsymbol{x} \in \Omega = [-5, 5]^3$.

Table 4. Initial conditions of the MHD variables for the Riemann problems.

	ρ	v_x	v_y	v_z	p	B^x	B^y	B^z
RP1, $x > 0$	0.125	0.0	0.0	0.0	0.1	0.5	− 1.0	0.0
RP1, $x \leq 0$	1.0	0.0	0.0	0.0	1.0	0.5	1.0	0.0
RP2, $x > 0$	1.0	− 0.45	− 0.2	0.2	1.0	2.0	− 0.7	0.5
RP2, $x \leq 0$	1.08	0.40	0.3	0.2	0.95	2.0	0.3	0.3

representation of the numerical results is offered in the right-hand panel of Fig. 4, which reports the numerical solution interpolated along 200 points at $z = 0$ and $y = x$ for the rest-mass density and the x-component of the velocity and of the magnetic field vectors as plotted against to the analytical solutions. Clearly, also in this case the numerical solution is shown to converge at the expected order of accuracy, confirming the validity of our implementation in the presence of a magnetic field and of a non-trivial coordinate mapping.

4.2 Non-smooth special-relativistic flows

The tests considered in this section are considerably different from those discussed so far in that they do not involve smooth flows and allow therefore for the presence of non-linear waves, either in the form of shocks or of steep gradients as those present at the fluid interface with an atmosphere.

4.2.1 Riemann problems

We start by considering two standard Riemann (or shock-tube) problems, here referred to, respectively, as RP1 and RP2, and originally proposed in the context of special relativistic MHD by Balsara (2001). Although these tests are solved on flat spatial hypersurfaces, i.e. $\gamma_{ij} = \delta_{ij}$, where δ_{ij} is the identity three-matrix, they employ different set-ups for the gauge variables, the lapse function and the shift vector. In particular, Table 4 provides all the considered initial conditions for the MHD variables of RP1 and RP2, while the lapse, the x-component of the shift, and the final time are chosen to be (α, β_x, $t_{\rm final}$) = (0.5, 0.0, 0.8), (1.0, 0.0, 0.4), (1.0, 0.4, 0.16), (2.0, 0.0, 0.2). The adiabatic index for RP1 and RP2 has been set to be $\Gamma = 2$ and $\Gamma = 5/3$, respectively.

For these tests, the HLL approximate Riemann solver has been used. Fig. 5 offers a 3D view of the rest-mass density variable for the proposed shock-tube problems and the corresponding AMR grid and limiting status, for the case $\alpha = 2$, obtained with our ADER-DG-$\mathbb{P}_3$ scheme using a level-zero mesh of 40×5 space elements on to with $\ell_{\rm max} = 2$ maximum refinement levels are added, and an ADER-DG-$\mathbb{P}_5$ scheme on a level-zero grid of 120×5 elements with one single refinement level $\ell_{\rm max} = 1$. The corresponding one-dimensional (1D) cuts relative to the $\mathbb{P}_5$ solutions are presented instead in Fig. 6 relatively to the test configurations listed in Table 4; shown with solid lines are the corresponding solutions from the exact Riemann solver of Giacomazzo & Rezzolla (2006). In the presence of moving discontinuities, the expected order of convergence of any shock capturing method is at most one. In Fig. 7, we show the results of a numerical convergence study for RP2, indicating that the numerical method converges indeed with the expected order of one for flows with shocks and discontinuities.

Overall, the results of these tests confirm the high-resolution shock-capturing capability, but also the robustness, of the new class of ADER-DG $\mathbb{P}_N$ schemes. In addition, they show that the *a posteriori* finite-volume subgrid limiter is activated only in very small portions of the domain and, in the case of genuine shocks, it is very narrowly concentrated near the discontinuity.

4.2.2 Advection of a 2D magnetic field loop

In this special-relativistic 2D problem, we advect a loop of magnetic field which is at a magnetic pressure much smaller than the corresponding fluid pressure. The computational domain in Cartesian coordinates is given by $(x, y) \in \Omega = [-1, +1] \times [-0.5, 0.5]$ with periodic boundary conditions everywhere. Using unitary (dimensionless) rest-mass density and gas pressure, i.e. $\rho = p = 1$, the velocity field is set to be constant with and initialized as

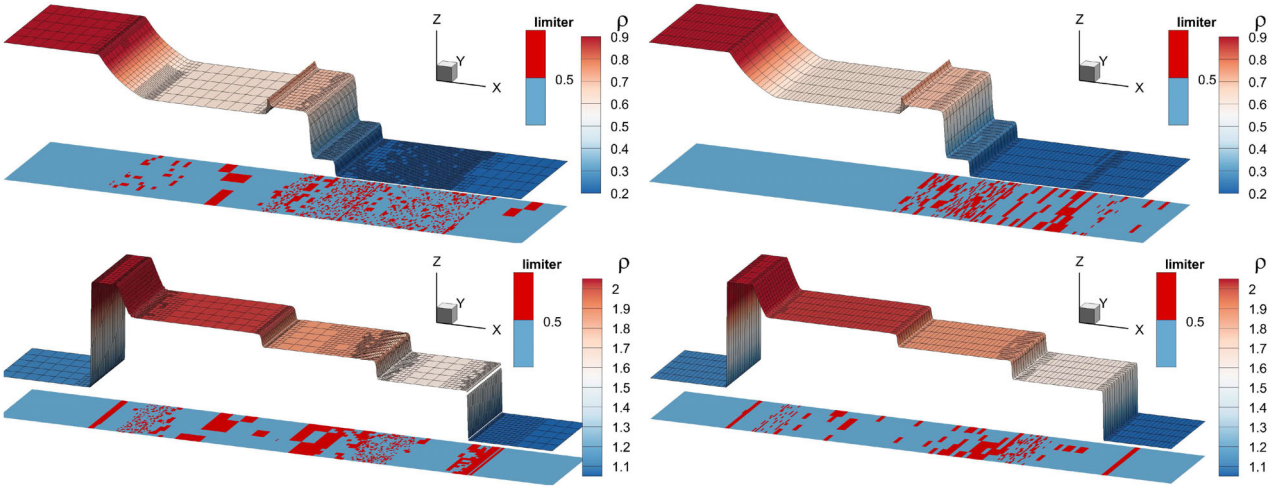

Figure 5. 3D view of the rest-mass density, the corresponding AMR grid and, on the horizontal plane, the corresponding limiting status, obtained with our ADER-DG $\mathbb{P}_N$ with finite-volume subcell limiting. From the top panel to the bottom, from left to right: (i) RP1 at $t_{\rm final} = 0.2$ with $\alpha = 2$, $\mathbb{P}_3$, with a coarsest grid of 40×5 elements, $\ell_{\rm max} = 2$; (ii) RP1 at $t_{\rm final} = 0.2$ with $\alpha = 2$, $\mathbb{P}_5$, with a coarsest grid of 120×5 elements, $\ell_{\rm max} = 1$; (iii) RP2 at $t_{\rm final} = 0.275$ with $\alpha = 2$, $\mathbb{P}_3$, with a coarsest grid of 40×5 elements, $\ell_{\rm max} = 2$; (iv) RP2 at $t_{\rm final} = 0.275$ with $\alpha = 2$, $\mathbb{P}_5$, with a coarsest grid of 120×5 elements, $\ell_{\rm max} = 1$. The limited cells, using the subcell ADER-TVD finite-volume scheme, are highlighted in red along the horizontal plane below the 3D plot of the rest-mass density ρ, while unlimited DG-$\mathbb{P}_N$ cells are highlighted in blue.

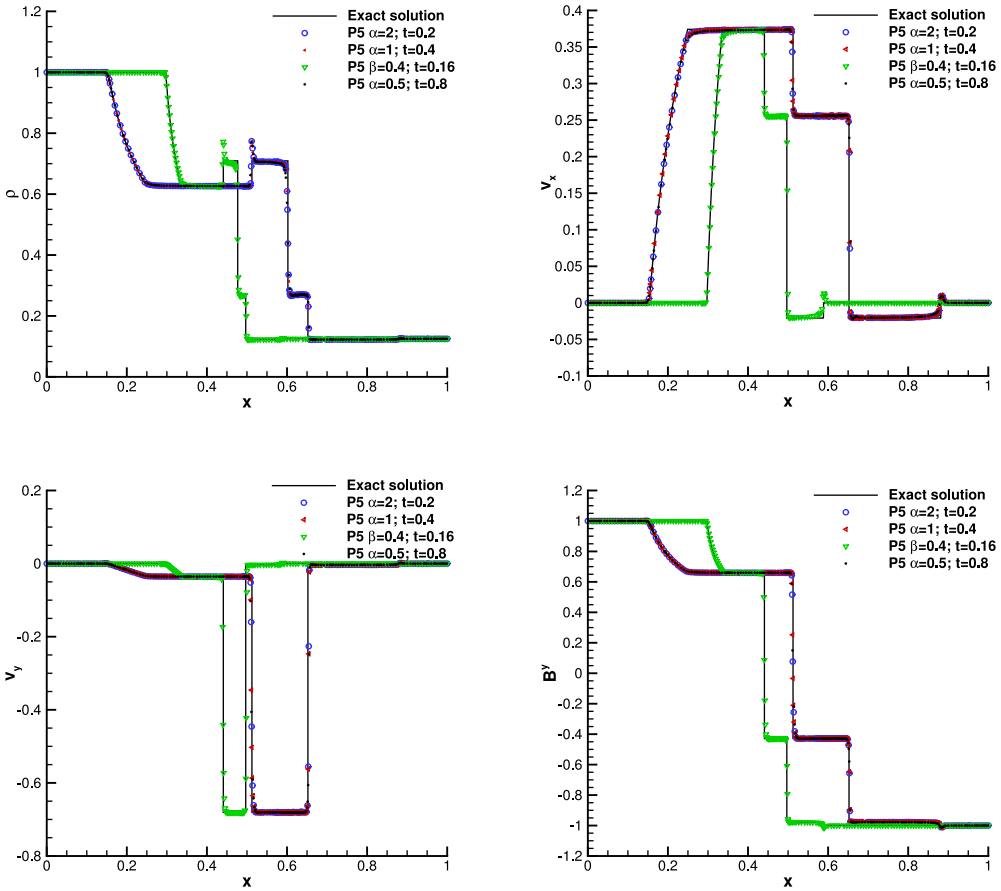

Figure 6. Riemann Problem 1 (RP1): the different panels show the various physical variables interpolated along a 1D cut, starting from a coarsest grid of 120×5 elements by using the ADER-DG-$\mathbb{P}_5$ scheme supplemented with the *a posteriori* ADER-TVD subcell and one single refinement level $\ell_{\rm max} = 1$. Shown with solid lines are the corresponding solutions from an exact Riemann solver.

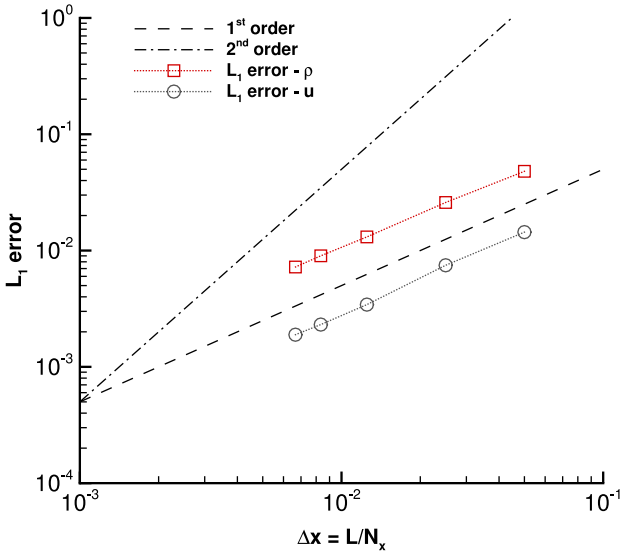

Figure 7. Convergence study against Riemann problem RP2 of Table 4. L_1 errors are plotted against the discretization step $\Delta x = L/N_x$, with $L = 1$ being the length of the 1D domain, N_x the discretization number, i.e. the number of high-order space elements in the x-direction. These tests have been performed with the fourth-order accurate ADER-DG-P3 scheme supplemented by our second-order subcell finite-volume limiter.

$(v_x, v_y) = (2, 1)V_0$, where $V_0 = 1/5$. The magnetic-field vector is derived from the magnetic vector potential, which is specified as

$$A_z = \begin{cases} A_0(R - r) & \text{for } r \le R, \\ 0 & \text{otherwise,} \end{cases} \tag{52}$$

where r is the radial coordinate, $R = 0.3$ is the radius of the advected loop, and the parameter $A_0 = 10^{-3}$ modules the magnetic field. The discontinuity at the loop boundaries has been initially slightly smoothed, e.g. by means of a standard linear smoothing in the form

$$B_x = \begin{cases} A_0 \frac{y}{r} & \text{for } r \le R, \\ s(r) A_0 \frac{y}{r} & \text{for } R < r \le R_1, \\ 0 & \text{otherwise.} \end{cases} \tag{53}$$

$$B_y = \begin{cases} -A_0 \frac{x}{r} & \text{for } r \le R, \\ -s(r) A_0 \frac{x}{r} & \text{for } R < r \le R_1, \\ 0 & \text{otherwise.} \end{cases} \tag{54}$$

where $s(r) = 1 - (r - R)/(r - R_1)$ is the adopted linear taper function, with R_1 chosen to be close to R, e.g. $R_1 = 0.315$.

Given the initial conditions and the periodic boundary conditions, the magnetic loop is advected across the computational domain and we have performed simulations using the lapse function set either to $\alpha = 1$ or to $\alpha = 2$, so that the corresponding simulation times to recover the initial configuration are $t = 5$ and $t = 2.5$, respectively; conversely, the shift vector β^i is set to zero.

This test has been solved using a level-zero mesh of 20^2 space elements with the maximum refinement levels $\ell_{\max} = 2$ via an ADER-DG-$\mathbb{P}_4$ scheme, supplemented with the *a posteriori* TVD SCL and by adopting an HLL Riemann solver. At this point, we would like to emphasize that instead of HLL or Rusanov-type Riemann solvers any other stable and monotone numerical flux could have been used equally well. The Riemann solver has to be understood as a building block of the DG scheme, exactly in the same way as it is in the finite-volume context. Fig. 8 reports the numerical results, which show a good agreement between the advected solution and the reference one given by the initial condition (left-hand panels). Furthermore, the limiter is only rarely activated, as expected for this test case (right-hand panels). The solutions for the divergence cleaning scalar ψ are plotted in Fig. 9.

4.2.3 2D blast wave

Another standard test of the RMHD equations is represented by the cylindrical blast wave problem. In this benchmark, the plasma is initially at rest and subject to a constant magnetic field along the

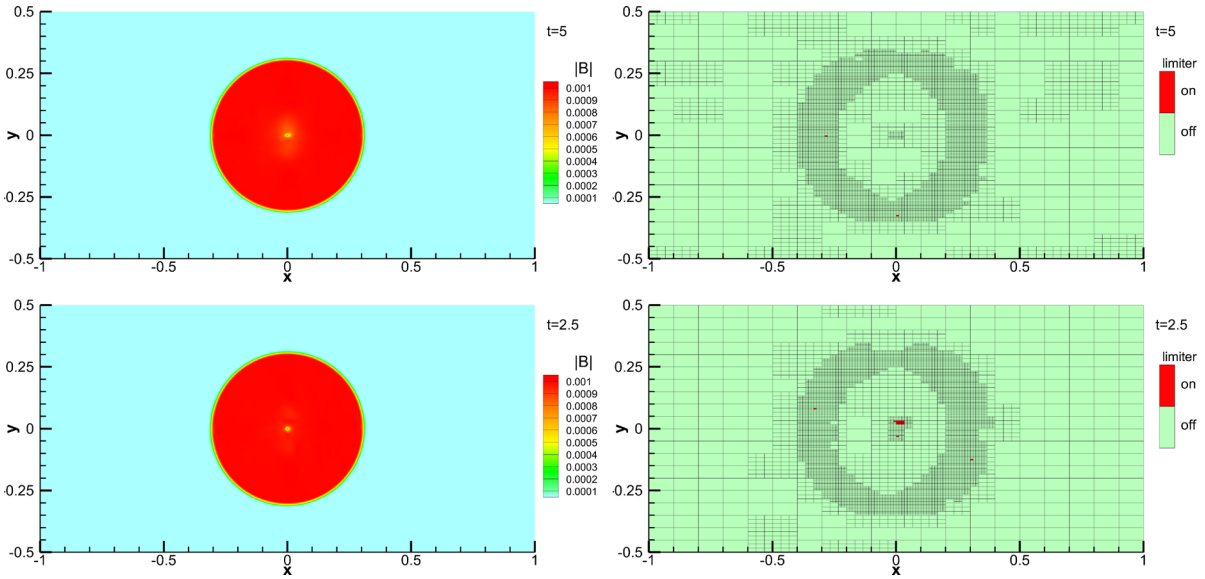

Figure 8. Advected magnetic field loop problem (SRMHD) obtained with the ADER-DG-$\mathbb{P}_4$ scheme supplemented with the *a posteriori* TVD SCL. Left-hand panels: $\mathbb{P}_4$-solution obtained for the magnetic field magnitude; right-hand panels: AMR-grid, troubled cells (red) and unlimited cells (green). Solution at time $t = 5.0$ with lapse function $\alpha = 1.0$ (top row) and at time $t = 2.5$ with lapse function $\alpha = 2$ (bottom row).

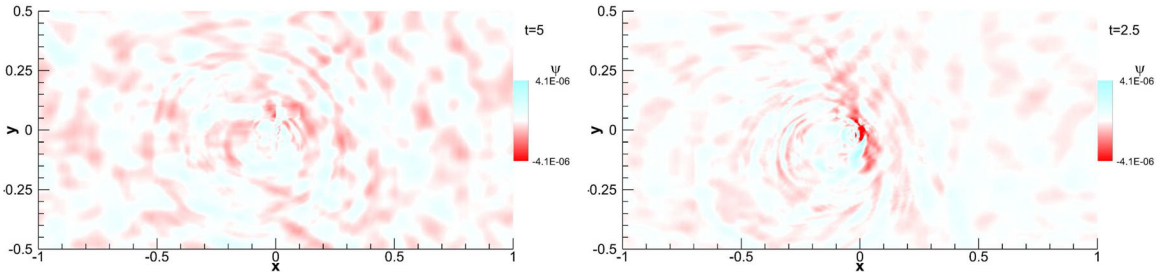

Figure 9. Advected magnetic field loop problem (SRMHD) obtained with the ADER-DG-$\mathbb{P}_4$ scheme supplemented with the *a posteriori* TVD SCL: results for the divergence cleaning scalar ψ at time $t = 5.0$ with lapse function $\alpha = 1.0$ (left) and at time $t = 2.5$ with lapse function $\alpha = 2$ (right).

x-direction; we have therefore considered two different configurations strengths of the magnetic field, i.e. $B_x = 0.1$ and $B_x = 0.5$, representing the case of a moderately and of a highly magnetized plasma, respectively.

The initial conditions for the rest-mass density and pressure are given respectively by

$$(\rho,\, p) = \begin{cases} (0.01,\, 1) & \text{if } r < R, \\ 10^{-4} \times (1,\, 5) & \text{otherwise,} \end{cases} \tag{55}$$

and together with the magnetic-field strength are sufficient to fully specify the initial setup. Also in this case, and following see Balsara & Spicer (1999), a linear smoothing is used in order to avoid sharp discontinuities in the initial conditions.

The computations have been carried out in 2D with a Cartesian coordinate system over a computational domain given by $\Omega = [-6, 6]^2$, with 40^2 elements on the coarsest mesh level, and a maximum refinement level $\ell_{\max} = 2$. We have used the Rusanov Riemann solver with our ADER-DG-$\mathbb{P}_3$ scheme. The computed results for different physical quantities, the AMR grid and the limiter status are shown in Fig. 10 for the moderately magnetized case, and in Fig. 11 for the highly magnetized case. Note in the bottom right-hand panels of figures the map of the 'troubled cells' and how these are limited in extent and nicely map the dynamics of the discontinuities in the magnetic field. Clearly, the fraction of troubled cells in the case of the low-magnetization set-up represent only a very small fraction of the evolved cells (see Fig. 10); this is to be contrasted with what happens in the case of the much more challenging case of high magnetization, where however the troubled cells still represent less than 50 per cent of the evolved cells (see Fig. 11).

Lacking an analytic solution to compare with, the assessment of the results in this case is harder, but it is reassuring that the results match well with those presented in other tests in the literature, e.g. by Del Zanna et al. (2007), Dionysopoulou et al. (2013), and Zanotti et al. (2015).

4.2.4 Orszag–Tang vortex

Our final special-relativistic test of non-smooth flows is another classic benchmark represented by the relativistic version of the Orszag–Tang vortex system (Orszag & Tang 1979). This is a useful application of our numerical infrastructure, as it involves the development of a complex and non-smooth magnetic-field structure and hence it explores geometries without trivial symmetries.

The initial conditions in this case are given by the vector of conserved variables

$$\begin{aligned} &\left(\rho, u, v, w, p, B_x, B_y, B_z\right) \\ &= \left(1, -\frac{3}{4\sqrt{2}}\sin y,\ \frac{3}{4\sqrt{2}}\sin x,\ 0,\ 1,\ -\sin y,\ \sin 2x,\ 0\right), \end{aligned}$$

with $\Gamma = 4/3$. The computational domain is $\Omega = [0, 2\pi]^2$, with 30^2 elements on the level-zero grid, a maximum refinement level of $\ell_{\max} = 2$, periodic boundary conditions, and a Rusanov Riemann solver for the subcell finite-volume limiter.

Fig. 12 shows the numerical results for the AMR grid with limiter status, the rest-mass density and the divergence-cleaning scalar ψ at different times, together with the corresponding numerical solution obtained with the same scheme on a fine uniform 270^2 mesh, corresponding to the finest mesh resolution at $\ell = \ell_{\max}$ and which serves here as a reference. The figure, in particular, refers to simulations in which the $\mathbb{P}_5$ version of our ADER-DG has been adopted. Also for this test, a rigorous accuracy analysis is not trivial but we note the very good agreement between the AMR simulations and the fine uniform-grid reference solution, as well as with the corresponding solutions that have been published elsewhere (see e.g. Zanotti et al. 2015; Porth et al. 2017). Note also how the AMR grid structure and the troubled-cells patterns closely follow the development of steeper gradients and discontinuities.

4.3 Non-smooth general-relativistic flows

In the following two sections, we discuss the use of our ADER-DG method in non-smooth general-relativistic flows, either in 2D and spherical coordinates or in 3D and Cartesian coordinates. The tests involve the evolution of non-self-gravitating tori as those presented in Section 4.2 with the important difference that the computational domain here fully contains the torus, whose exterior is therefore filled with a uniform atmosphere at a rest-mass density of $\rho_0 = 10^{-9}$ that is five orders of magnitude smaller than the one at the torus centre.

4.3.1 2D torus around a Schwarzschild black hole

First, we consider a thick torus in equilibrium orbiting around a black hole with the parameters previously described in Section 4.1.2 and using horizon-penetrating spherical KS coordinates in 2D. The computational domain $(r,\, \theta) \in \Omega = [2,\, 18] \times [0.5,\, 2.5]$ is discretized with a uniform mesh of 50^2 elements using an ADER-DG-$\mathbb{P}_3$ scheme with TVD subcell finite-volume limiter (as a comparison, the torus has an inner radius $r_{\rm in} = 5.5$ and an outer radius $r_{\rm out} = 13.8$, so that the entire torus is resolved with only 26 elements in radial direction and 14 elements in angular direction). On the outer edge, we impose the initial data as boundary condition in all variables.

A 1D cut of the rest-mass density in the radial direction is shown in the left-hand panel of Fig. 13 and is plotted over the analytic solution at $t = 100\,M$. Note the excellent agreement between the numerical results and the exact solution, with differences in the central rest-mass density that are less than 0.7 per cent.

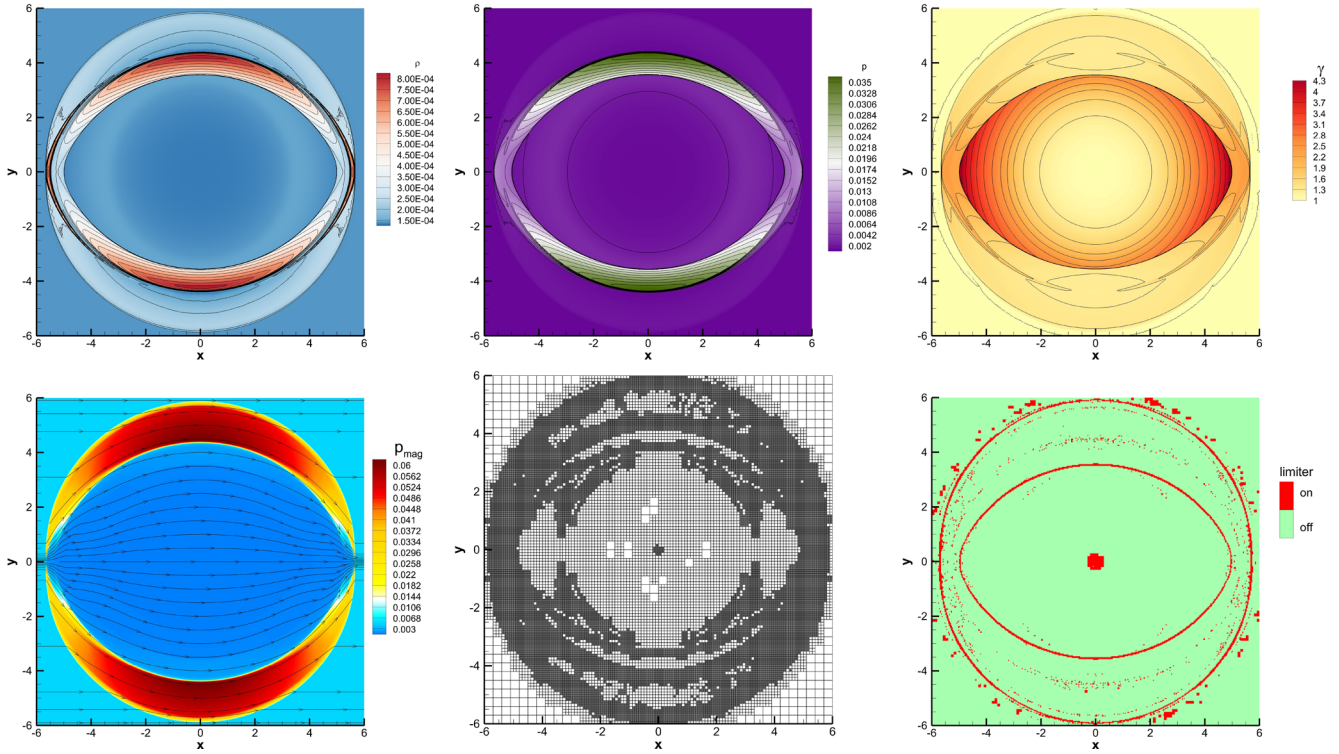

Figure 10. Solution of the SRMHD blast wave with $B_x = 0.1$ at time $t = 4.0$, obtained with the ADER-DG $\mathbb{P}_3$ scheme supplemented with the *a posteriori* second-order TVD SCL. Top panels: rest-mass density (left), thermal pressure (centre), and Lorentz factor (right). Bottom panels: magnetic pressure (left) with magnetic field lines reported, AMR grid (centre) and limiter map (right) with troubled cells marked in red and regular unlimited cells marked in green.

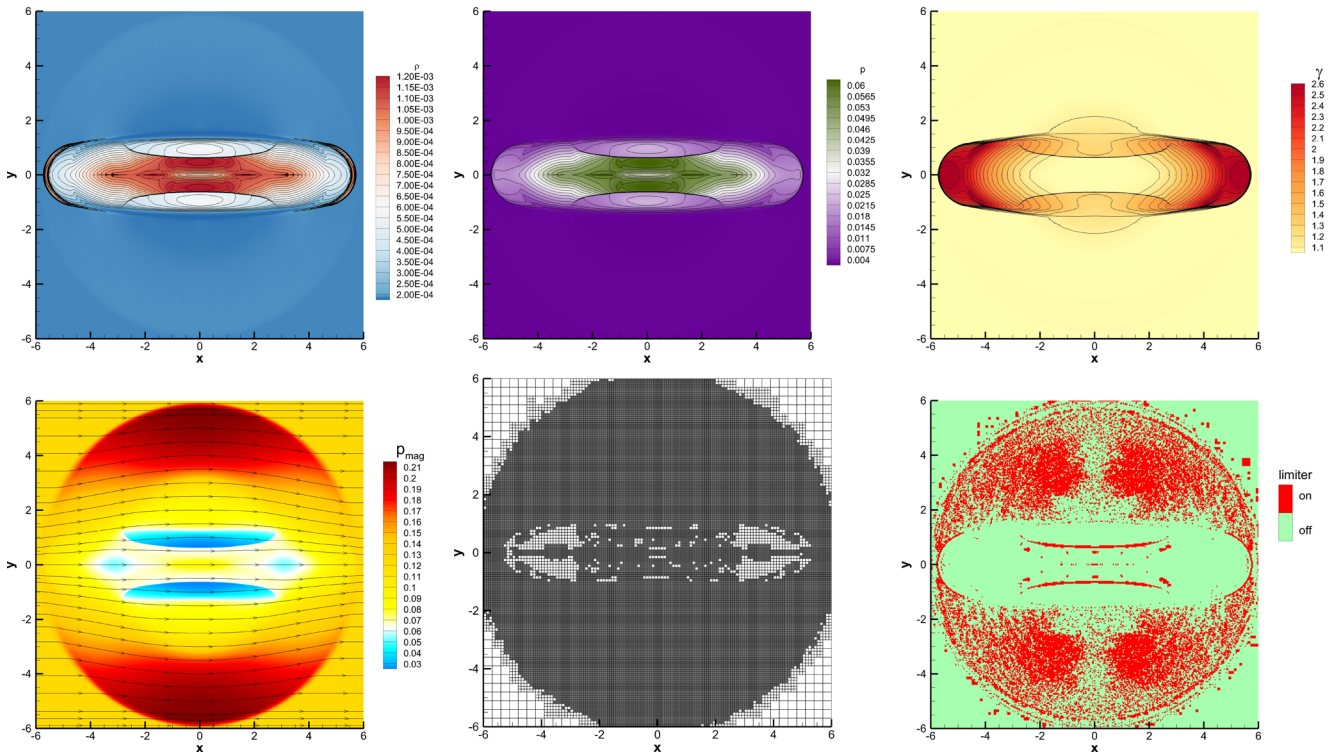

Figure 11. Solution of the SRMHD blast wave with $B_x = 0.5$ at time $t = 4.0$, obtained with the ADER-DG $\mathbb{P}_3$ scheme supplemented with the *a posteriori* second-order TVD SCL. Top panels: rest-mass density (left), thermal pressure (centre), and Lorentz factor (right). Bottom panels: magnetic pressure (left) with magnetic field lines reported, AMR grid (centre), and limiter map (right) with troubled cells marked in red and regular unlimited cells marked in green.

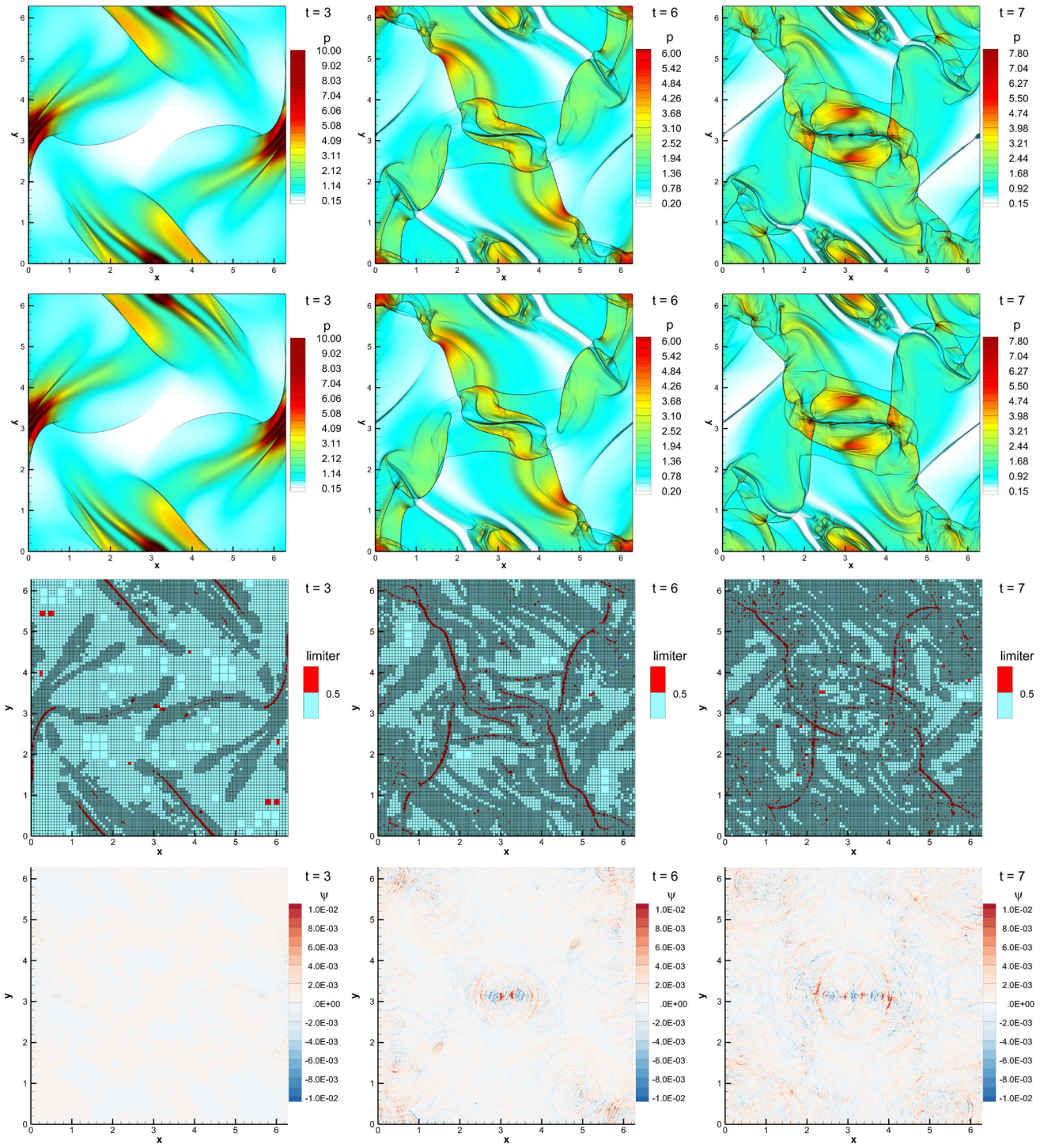

Figure 12. SRMHD Orszag–Tang vortex problem at times $t = 3$, $t = 6$, $t = 7$, from left to right, obtained through the ADER-DG-$\mathbb{P}_5$ scheme supplemented with the *a posteriori* TVD SCL on a 30^2 elements on the coarsest grid ($\ell = 0$), two maximum refinement levels and a refinement factor $\mathcal{R} = 3$. From the top to the bottom row: (i) $\mathbb{P}_5$ solution obtained on the AMR grid; (ii) $\mathbb{P}_5$ solution obtained on the corresponding finer uniform grid, i.e. 270^2 space elements of the maximum refinement level $\ell_{\max} = 2$; (iii) AMR grid, troubled cells (red) and unlimited cells (blue); and (iv) divergence cleaning scalar ψ.

It is useful to remark that the low-density atmosphere has been successfully simulated and robustly evolved in time with a high-order ADER-DG scheme and that inside the computational domain the limiter is activated only on the border of the torus, where spurious oscillations may generate possibly negative-valued densities and pressures in the high-order DG polynomials. However, the *a posteriori* subcell finite-volume limiter appears to be robust enough to accurately treat the atmosphere of the torus. Furthermore, we note that the fluid in this low-density region is treated so as to be evolved as a standard fluid, i.e. the velocity is not set to zero in a computational cell that is marked to host the atmosphere. As a result, during the simulations, the fluid in the atmosphere starts accreting on to the black hole; in practice, the amount of matter accreted in this manner is minute and does not get

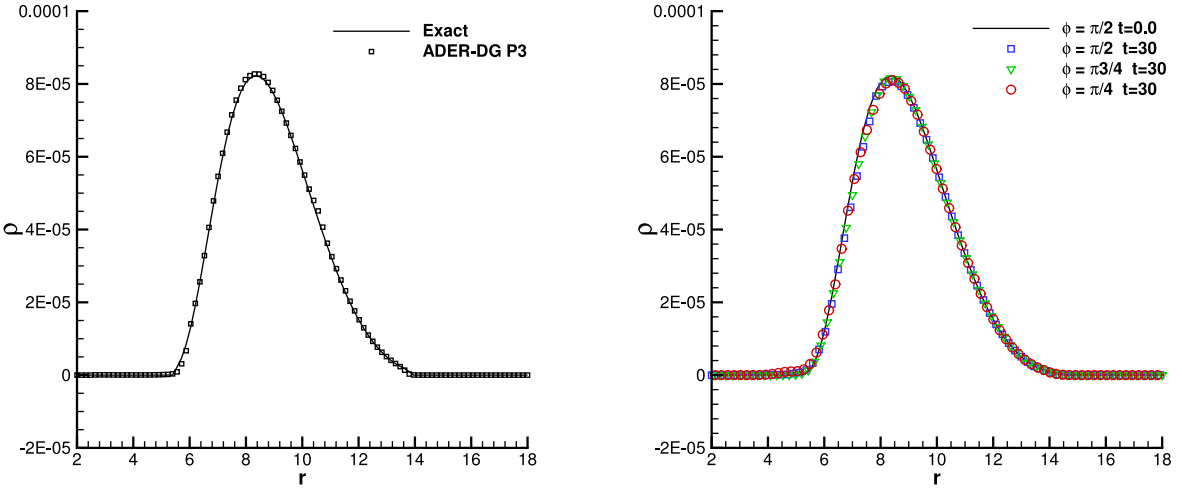

Figure 13. Results obtained with the ADER-DG $\mathbb{P}_3$ scheme supplemented with the *a posteriori* second-order TVD SCL. 1D cut and comparison with the exact solution. 2D simulation of the torus in spherical KS coordinates at time $t = 100$ (left), and 3D simulation in Cartesian KS coordinates at time $t = 30$ for different azimuthal angles (right).

influenced with the dynamics of the much denser matter lost from the torus.

4.3.2 3D torus around a Schwarzschild black hole

The final test considered in this battery is represented by a fully 3D evolution of the torus considered in the previous section, therefore adding the azimuthal spatial dimension.

For this, we use a horizon-penetrating Cartesian KS coordinates that cover a computational domain chosen to be $(x, y, z) \in \Omega = [-18, +18] \times [2, 18] \times [-8, +8]$. The portion of the domain around the origin is excised following the same logic discussed in Section 4.1.3. The solution has been computed using an ADER-DG-$\mathbb{P}_3$ scheme on a uniform mesh composed of $40 \times 20 \times 20$ elements.

The 1D cut of the rest-mass density profile on the equatorial plane $\theta = \pi/2$ and along different angular directions $\phi = \pi/4, \pi/2$, and $3\pi/4$ at $t \sim 30\,M$. The various numerical solutions are overlayed with the corresponding analytic solutions in the right-hand panel of Fig. 13. Once again, we can observe an excellent agreement between numerical and exact solution, with differences in the central rest-mass density that are less than 1.5 per cent.

5 STRONG MPI SCALING AND PERFORMANCE COMPARISON WITH OTHER SCHEMES

In this section, we provide a detailed and quantitative performance analysis of the new ADER-DG schemes for the GRMHD equations proposed in this paper. We compare CPU times and MPI scaling results for ADER-DG in comparison with classical RKDG schemes. We furthermore provide CPU time comparisons between ADER-DG and ADER-WENO finite-volume (FV) methods.

As first test we run the Michel accretion problem again on the domain $\Omega = [3, 5.5] \times [1, \pi - 1]$ in two space dimensions using a sequence of successively refined meshes of $N_x \times N_x$ DG elements and $N_x(N+1) \times N_x(N+1)$ finite-volume zones until a final time of $t = 10$. We use a third-order ADER-DG scheme ($N = 2$) and compare with a third-order ADER-WENO finite-volume scheme (see Dumbser et al. 2008b; Dumbser et al. 2013). In order to make the comparison fair, the mesh of the FV scheme is $N+1$ times finer than the one of the DG scheme, since the DG method has $N+1$ degrees of freedom per cell and per space dimension. The total number of degrees of freedom is therefore the same for both methods. We present the L_2 and L_∞ errors for the density ρ obtained with both methods. We also report the wall clock time (WCT) measured in seconds and the time needed by the scheme to update one single degree of freedom on one single CPU core (DTU), measured also in seconds. The inverse of this number represents the number of degrees of freedom that the scheme is able to update in one second on one CPU core and can be compared with other finite-volume and finite-difference methods. As computer hardware for this test we use one single CPU core of a workstation with an Intel i7-4770 CPU with 3.4 GHz clock speed and 16GB of RAM. The results are shown in Table 5, from which it becomes clear that the ADER-DG scheme is faster and more accurate than the ADER finite-volume scheme using the same number of degrees of freedom. Similar results have already been reported in Dumbser et al. (2008b) and Dumbser (2010) for the Euler equations of hydrodynamics, the MHD equations and the compressible Navier–Stokes equations, using the unified framework of $P_N P_M$ schemes.

Table 5. Comparison of L_2 and L_∞ errors for the Michel accretion problem in 2D. WCTs and CPU time per degree of freedom update (TDU) in seconds for a third-order ADER-DG scheme ($N = 2$) compared with a third-order ADER-WENO finite-volume (FV) scheme.

	N_x	L_2 error	L_∞ error	WCT (s)	TDU (s)
DG $\mathcal{O}3$	6	2.53E−05	3.26E−05	15.9	1.0470E−04
	12	3.32E−06	4.46E−06	74.4	6.3726E−05
	18	1.01E−06	1.37E−06	193.5	4.9770E−05
	30	2.26E−07	3.07E−07	733.4	4.1173E−05
FV $\mathcal{O}3$	18	2.77E−05	5.99E−05	37.7	5.1765E−04
	36	6.40E−06	1.72E−05	231.9	4.0117E−04
	54	2.73E−06	8.81E−06	694.0	3.5679E−04
	90	9.44E−07	3.78E−06	2754.8	3.0694E−04

As second test case we take the large amplitude Alfvén wave problem in flat Minkowski space–time described in Del Zanna et al. (2007) and also used later in Dumbser et al. (2008b) and Zanotti & Dumbser (2015). We use the 3D computational domain $\Omega = [0, 2\pi]^3$, which is discretized with ADER-DG schemes of

Table 6. Accuracy and cost comparison between ADER-DG and RK-DG schemes of different orders for the GRMHD equations in three-space dimensions. The test problem is the large amplitude Alfvén wave solved in the domain $\Omega = [0, 2\pi]^3$ up to $t = 1$ on a sequence of successively refined Cartesian meshes with N_x^3 elements. The errors refer to the variable B_y. The table also contains total WCTs measured in seconds and the time needed by the scheme to update one single degree of freedom on one single CPU core (TDU) measured in microseconds. All simulations have been performed in parallel on 512 MPI ranks of the SuperMUC phase I system at the LRZ in Garching, Germany. Note that for the coarsest grid with $N_x = 8$, each MPI rank has only one single element to update.

N_x	L_2 error	L_2 order	WCT (s)	TDU (μs)	N_x	L_2 error	L_2 order	WCT (s)	TDU (μs)
		ADER-DG ($N = 3$)					RK-DG ($N = 3$)		
8	7.6396E−04		0.093	33.8	8	8.0909E−04		0.107	39.2
16	1.7575E−05	5.44	1.371	31.5	16	2.2921E−05	5.14	1.394	32.0
24	6.7968E−06	2.34	6.854	31.0	24	7.3453E−06	2.81	6.894	31.2
32	1.0537E−06	6.48	21.642	31.1	32	1.3793E−06	5.81	21.116	30.3
		ADER-DG ($N = 4$)					RK-DG ($N = 4$)		
8	6.6955E−05		0.363	46.8	8	6.8104E−05		0.456	51.4
16	2.2712E−06	4.88	5.696	45.9	16	2.3475E−06	4.86	6.666	51.0
24	3.3023E−07	4.76	28.036	44.9	24	3.3731E−07	4.78	29.186	45.3
32	7.4728E−08	5.17	89.271	45.2	32	7.7084E−08	5.13	87.115	43.4
		ADER-DG ($N = 5$)					RK-DG ($N = 5$)		
8	5.2967E−07		1.090	53.1	8	5.7398E−07		1.219	55.9
16	7.4886E−09	6.14	16.710	51.2	16	8.1461E−09	6.14	17.310	52.5
24	7.1879E−10	5.78	84.425	51.2	24	7.7634E−10	5.80	83.777	49.4
32	1.2738E−10	6.01	263.021	50.3	32	1.3924E−10	5.97	260.859	49.5

increasing order of accuracy in space and time and using a sequence of successively refined meshes of size $N_x \times N_x \times N_x$. To provide a direct a comparison, we solve the same test problem also with high-order RK-DG schemes (Cockburn & Shu 1998b, 2001). Since ADER-DG schemes are uniformly high-order accurate in space and time, for the RK-DG method we use appropriate RK schemes in time whose temporal order of accuracy exactly matches the spatial one. In particular, we use the classical third and fourth-order RK schemes of Kutta (1901), the fifth order RK scheme of Fehlberg (1969), and the first one of the sixth-order RK schemes proposed in Butcher (1964). Note that due to the well-known Butcher barriers that apply to high-order RK schemes for non-linear ODE systems, the fifth-order RK scheme has six stages, and the sixth-order RK scheme has seven stages. We run the test problem with both schemes without any limiter up to a final time of $t = 1$ and report the errors of the variable B_y measured in L_2 norm.

The computational results for ADER-DG and RK-DG schemes are reported in Table 6, together with the measured WCTs in seconds and the time needed by each scheme to update one single degree of freedom (TDU) in microseconds. Again, the inverse of TDU in seconds represents the number of degrees of freedom that the scheme is able to update in one second on one single CPU core and can be directly compared with existing finite-volume and finite-difference codes. We observe that the CPU times and error norms are comparable for both schemes. For all mesh sizes N_x and polynomial approximation degrees N we have used 512 CPU cores of the Phase I system of the SuperMUC of the LRZ in Garching, Germany. This means that for the coarsest mesh with $N_x = 8$, each MPI rank has only one single element to update. The results of Table 6 clearly show that for a small number of elements per MPI rank our *communication avoiding* ADER-DG schemes are computationally less expensive than RK-DG schemes of the same order, since RK-DG requires MPI communication in each RK stage. We finally run this test problem on a fixed grid of 64 000 elements ($N_x = 40$) using fourth-order ADER-DG and RK-DG schemes on an increasing number of CPUs, from 64 to 16 000. The parallel implementation is based on pure MPI and thus each CPU core corresponds to one MPI rank. The speed-up graph and the parallel efficiency as measured

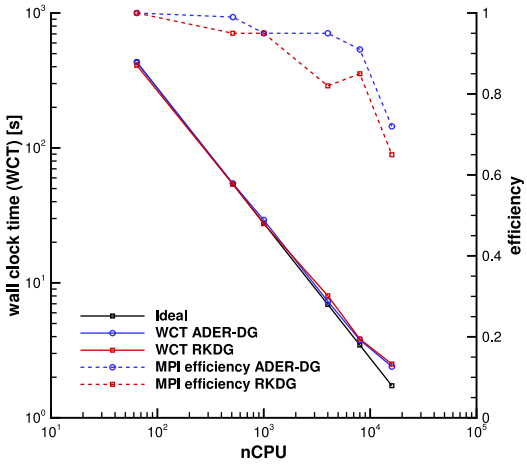

Figure 14. Strong scaling test for the 3D GRMHD equations and performance comparison between fourth-order ADER-DG and RK-DG schemes ($N = 3$). The test case is the large amplitude Alfvén wave problem solved in 3D up to $t = 1$ on a uniform Cartesian mesh composed of $40 \times 40 \times 40$ elements. The results were obtained with a pure MPI implementation on the SuperMUC phase I system at the LRZ in Garching, Germany, using 64 to 16 000 CPU cores. On 16k cores, each MPI rank has only four elements to update.

on the Phase I system of the SuperMUC supercomputer of the LRZ in Garching, Germany, are presented in Fig. 14. It shows the better MPI scaling of the communication avoiding ADER-DG schemes compared to conventional RK-DG methods.

6 DISCUSSION AND CONCLUSIONS

We have proposed a new high-order DG scheme for the numerical solution of the system of the GRMHD equations in the ideal-MHD limit using multiple spatial dimensions and on space–time adaptive meshes. An important and novel aspect of our discretization is that we have made use of non-conservative products in order to account for the metric terms directly inside the Riemann solver

at the element interfaces instead of considering them as purely algebraic source terms. While there is no development yet of exactly well-balanced numerical schemes for GRMHD for some relevant stationary equilibrium solutions, our approach here is motivated by the encouraging results already obtained in this respect by Parés (2006), Castro et al. (2006), and Dumbser et al. (2009), who have employed the framework of well-balanced path-conservative finite-volume and DG schemes for the successful solution of the shallow-water equations. One of the main feature of our ADER-DG scheme is its ability to reach arbitrary high order of accuracy in space and time for smooth parts of the solution, while it falls back to a robust finite-volume scheme at discontinuities such as shocks and material interfaces, without losing the subcell resolution capabilities of the high-order DG scheme.

We have validated the numerical implementation of the novel ADER-DG scheme with an *a posteriori* subcell finite-volume limiter by solving the system of GRHD and GRMHD equations in the ideal-MHD limit for a number of classical benchmark tests. These tests have been performed both in 2D and in 3D with either spherical or Cartesian coordinate mappings. Furthermore, they have involved either smooth relativistic flows, for which we have been able to compute the convergence order and compare it with the expected one, or non-smooth relativistic flows, for which we have been able to compare our results with exact solutions or other reference solutions available in the literature. Overall, the benchmarks have shown a very good performance of the new scheme, exhibiting an excellent agreement between analytical and numerical solutions and that the latter converge at the expected and high order for smooth flows.

The developments presented here on the solution of the GRMHD equations is part of a long-term plan to develop a numerical infrastructure for the study of problems in relativistic astrophysics in general and to simulate the merger of binary systems of neutron stars in particular [see e.g. Baiotti & Rezzolla (2017) for a recent review]. Indeed, another important development in this respect has been the successful development and testing of a first-order hyperbolic formulation of the Einstein equations, given by the first-order reduction of the CCZ4 system (Alic et al. 2012), which was recently presented by Dumbser et al. (2018) (FO-CCZ4). These two independent but related developments naturally lead to the construction of a computational framework, where the GRMHD equations are evolved *together* with the Einstein field equations in a fully coupled manner. This is one of the goals of the ExaHyPE framework (Charrier & Weinzierl 2018; Köppel 2017; Charrier et al. 2018) and is part of our present and future research. The key idea here is to use our new ADER-DG schemes to solve the GRMHD equations and the FO-CCZ4 formulation of the Einstein equations *together*, i.e. in a *monolithically coupled* way, simulating with the same numerical scheme one single evolution system for both matter and space–time.

We also plan to carry out an extension to full general relativity of the first-order symmetric hyperbolic model of continuum mechanics recently proposed by Peshkov & Romenski (2016), Dumbser et al. (2016), and Dumbser et al. (2017), and which is based on the pioneering work of Godunov & Romenski (1972) on non-linear hyperelasticity in the Newtonian limit. This new unified formulation of continuum mechanics allows one to deal with viscous fluids and elastic solids within one single and unified system of symmetric-hyperbolic partial differential equations and has bounded signal speeds for all involved physical processes, including dissipative effects. In addition, this mathematical development will be accompanied by a numerical one, with the implementation of a novel indicator for AMR and subcell limiting based on the definition of the numerical entropy density and relative fluxes as done, e.g. by Puppo & Semplice (2011), Semplice et al. (2016), and Cravero & Semplice (2016).

ACKNOWLEDGEMENTS

We are grateful to Bruno Giacomazzo for the numerical code used for the exact solution of the Riemann problem in RMHD and to Luca Del Zanna for the useful suggestions about the initial conditions of the stationary torus. We also thank the anonymous referee for valuable suggestions and constructive comments. This research was funded by the European Union's Horizon 2020 Research and Innovation Programme under the project *ExaHyPE*, grant no. 671698 (call FETHPC-1-2014) and was also supported by the European Research Council (ERC) synergy grant 'BlackHoleCam' (grant no. 610058), by 'NewCompStar', COST Action MP1304, by the LOEWE-Programme in the Helmholtz International Center (HIC) for FAIR. The simulations were performed on the SuperMUC supercomputer at the LRZ in Garching, Germany, on the LOEWE cluster in Center for Scientific Computing (CSC) in Frankfurt, on the HazelHen supercomputer at the HLRS in Stuttgart, Germany, as well as on the local HPC cluster at the University of Trento.

REFERENCES

Abramowicz M., Jaroszynski M., Sikora M., 1978, A&A, 63, 221
Alic D., Bona-Casas C., Bona C., Rezzolla L., Palenzuela C., 2012, Phys. Rev. D, 85, 064040
Aloy M., Cordero-Carrión I., 2016, J. Phys. Conf. Ser., 719, 12015
Anderson M., Hirschmann E. W., Lehner L., Liebling S. L., Motl P. M., Neilsen D., Palenzuela C., Tohline J. E., 2008, Phys. Rev. Lett., 100, 191101
Anile A. M., 1990, Relativistic Fluids and Magneto-fluids. Cambridge Univ. Press, Cambridge
Anninos P., Fragile P. C., Salmonson J. D., 2005, ApJ, 635, 723
Anninos P., Bryant C., Fragile P., Holgado A., Lau C., Nemergut D., 2017, ApJS, 231, 17
Antón L., Zanotti O., Miralles J. A., Martí J. M., Ibáñez J. M., Font J. A., Pons J. A., 2006, ApJ, 637, 296
Baiotti L., Rezzolla L., 2017, Rept. Prog. Phys., 80, 096901
Baiotti L., Hawke I., Montero P. J., Löffler F., Rezzolla L., Stergioulas N., Font J. A., Seidel E., 2005, Phys. Rev. D, 71, 024035
Balsara D., 2001, ApJS, 132, 83
Balsara D., Kim J., 2016, J. Comput. Phys., 312, 357
Balsara D. S., Spicer D., 1999, J. Comput. Phys., 148, 133
Balsara D. S., Altmann C., Munz C., Dumbser M., 2007, J. Comput. Phys., 226, 586
Balsara D., Meyer C., Dumbser M., Du H., Xu Z., 2013, J. Comput. Phys., 235, 934
Baumgarte T. W., Shapiro S. L., 2003, ApJ, 585, 921
Berger M. J., Colella P., 1989, J. Comput. Phys., 82, 64
Berger M. J., Jameson A., 1985, AIAA J., 23, 561
Berger M. J., Oliger J., 1984, J. Comput. Phys., 53, 484
Bermúdez A., Vázquez M., 1994, Comput. Fluids, 23, 1049
Bucciantini N., Del Zanna L., 2011, A&A, 528, A101
Bucciantini N., Zanna L. D., 2013, MNRAS, 428, 71
Bugli M., Del Zanna L., Bucciantini N., 2014, MNRAS, 440, L41
Bugner M., Dietrich T., Bernuzzi S., Weyhausen A., Brügmann B., 2016, Phys. Rev. D, 94, 084004
Bungartz H., Mehl M., Neckel T., Weinzierl T., 2010, Comput. Mech., 46, 103
Butcher J., 1964, J. Aust. Math. Soc., 4, 179
Casoni E., Peraire J., Huerta A., 2013, Int. J. Numer. Methods Fluids, 71, 737

Castro M., Gallardo J., Parés C., 2006, Math. Comput., 75, 1103
Castro M., Pardo A. Parés C., Toro E., 2010, Math. Comput., 79, 1427
Cesenek J., Feistauer M., Horacek J., Kucera V., Prokopova J., 2013, Appl. Math. Comput., 219, 7139
Charrier D. E., Weinzierl T., 2018, preprint (arXiv:1801.08682)
Charrier D. E. et al., 2018, ExaHyPE, an Exascale Hyperbolic PDE Engine. Available at: http://www.exahype.eu
Clain S., Diot S., Loubère R., 2011, J. Comput. Phys., 230, 4028
Cockburn B., Shu C. W., 1998a, J. Comput. Phys., 141, 199
Cockburn B., Shu C., 1998b, J. Comput. Phys., 141, 199
Cockburn B., Shu C., 2001, J. Sci. Comput., 16, 173
Cockburn B., Lin S., Shu C., 1989, J. Comput. Phys., 84, 90
Cockburn B., How S., Shu C., 1990, Math. Comp., 54, 545
Cockburn B., Karniadakis G. E., Shu C.-W., 2000, Discontinuous Galerkin Methods: Theory, Computation and Applications. Lecture Notes on Computational Science and Engineering. Springer-Verlag, Berlin, Heidelberg
Cravero I., Semplice M., 2016, J. Sci. Comput., 67, 1219
Dal Maso G., LeFloch P. G., Murat F., 1995, J. Math. Pures Appl., 74, 483
Dedner A., Kemm F., Kröner D., Munz C.-D., Schnitzer T., Wesenberg M., 2002, J. Comput. Phys., 175, 645
Del Zanna L., Zanotti O., Bucciantini N., Londrillo P., 2007, A&A, 473, 11
Dionysopoulou K., Alic D., Palenzuela C., Rezzolla L., Giacomazzo B., 2013, Phys. Rev. D, 88, 044020
Diot S., Clain S., Loubère R., 2012, Comput. Fluids 64, 43
Duez M. D., Liu Y. T., Shapiro S. L., Stephens B. C., 2005, Phys. Rev. D, 72, 024028
Dumbser M., 2005, Arbitrary High Order Schemes for the Solution of Hyperbolic Conservation Laws in Complex Domains. Shaker Verlag, Aachen
Dumbser M., 2010, Comput. Fluids, 39, 60
Dumbser M., Balsara D. S., 2016, J. Comput. Phys., 304, 275
Dumbser M., Toro E. F., 2011, J. Sci. Comput., 48, 70
Dumbser M., Zanotti O., 2009, J. Comput. Phys., 228, 6991
Dumbser M., Schwartzkopff T., Munz C., 2006, Computational Science and High Performance Computing II. Notes on Numerical Fluid Mechanics and Multidisciplinary Design (NNFM). Springer-Verlag, Berlin, Heidelberg, p. 129
Dumbser M., Enaux C., Toro E., 2008a, J. Comput. Phys., 227, 3971
Dumbser M., Balsara D. S., Toro E. F., Munz C.-D., 2008b, J. Comput. Phys., 227, 8209
Dumbser M., Castro M., Parés C., Toro E., 2009, Comput. Fluids, 38, 1731
Dumbser M., Zanotti O., Hidalgo A., Balsara D., 2013, J. Comput. Phys., 248, 257
Dumbser M., Hidalgo A., Zanotti O., 2014a, Comput. Methods Appl. Mech. Eng., 268, 359
Dumbser M., Zanotti O., Loubère R., Diot S., 2014b, J. Comput. Phys., 278, 47
Dumbser M., Peshkov I., Romenski E., Zanotti O., 2016, J. Comput. Phys., 314, 824
Dumbser M., Peshkov I., Romenski E., Zanotti O., 2017, J. Comput. Phys., 348, 298
Dumbser M., Guercilena F., Köppel S., Rezzolla L., Zanotti O., 2018, Phys. Rev. D, preprint (arXiv:1707.09910)
Einfeldt B., Munz C. D., Roe P. L., Sjögreen B., 1991, J. Comput. Phys., 92, 273
Etienne Z. B., Liu Y. T., Shapiro S. L., 2010, Phys. Rev. D, 82, 084031
Fambri F., Dumbser M., 2016, Appl. Numer. Math., 110, 41
Fambri F., Dumbser M., Zanotti O., 2017, Comput. Phys. Commun., 220, 297
Fechter S., Munz C.-D., 2015, Int. J. Numer. Methods Fluids, 78, 413
Fehlberg E., 1969, Computing, 4, 93
Font J. A., 2008, Living Rev. Relativ., 6, 4; http://www.livingreviews.org/lrr
Font J. A., Daigne F., 2002, MNRAS, 334, 383
Gaburro E., Dumbser M., Castro M., 2017, Comput. Fluids, 159, 254
Gaburro E., Castro M. J., Dumbser M., 2018, MNRAS, 477, 2251
Galerkin B. G., 1915, Vestnik Inzhenerov i Tekhnikov, 19, 897
Gammie C. F., McKinney J. C., Tóth G., 2003, ApJ, 589, 458
Gassner G., Dumbser M., Hindenlang F., Munz C., 2011, J. Comput. Phys., 230, 4232
Giacomazzo B., Rezzolla L., 2006, J. Fluid Mech., 562, 223
Giacomazzo B., Rezzolla L., 2007, Class. Quantum Gravity, 24, S235
Godunov S. K., 1959, Mat. Sb., 47, 271
Godunov S., Romenski E., 1972, J. Appl. Mech. Tech. Phys., 13, 868
Gourgoulhon E., 2012, 3+1 Formalism in General Relativity. Lecture Notes in Physics, Vol. 846. Springer-Verlag, Berlin
Hartmann R., Houston P., 2002, J. Comp. Phys., 183, 508
Hidalgo A., Dumbser M., 2011, J. Sci. Comp., 48, 173
Jiang G., Shu C., 1994, Math. Comput., 62, 531
Khokhlov A., 1998, J. Comput. Phys., 143, 519
Kidder L. et al., 2017, J. Comput. Phys., 335, 84
Kiuchi K., Sekiguchi Y., Shibata M., Taniguchi K., 2009, Phys. Rev. D, 80, 064037
Komissarov S. S., 1999, MNRAS, 303, 343
Komissarov S. S., 2004, MNRAS, 350, 1431
Köppel S., 2017, preprint (arXiv:1711.08221)
Kozlowski M., Jaroszynski M., Abramowicz M. A., 1978, A&A, 63, 209
Krivodonova L., 2007, J. Comput. Phys., 226, 879
Kutta W., 1901, Zeit. Math. Physik, 46, 435
Löhner R., 1987, Comput. Methods Appl. Mech. Eng., 61, 323
Loubère R., Dumbser M., Diot S., 2014, Commun. Comput. Phys., 16, 718
Luo H., Baum J. D., Löhner R., 2007, J. Comput. Phys., 225, 686
Martí J. M., Müller E., 2015, Living Rev. Comput. Astrophys., 1, 3
Meister A., Ortleb S., 2016, Appl. Math. Comput., 272, 259
Michel F. C., 1972, Astrophys. Spa. Sci., 15, 153
Miller J., Schnetter E., 2017, Class. Quantum Gravity, 34, 015003
Misner C. W., Thorne K. S., Wheeler J. A., 1973, Gravitation. W. H. Freeman, San Francisco
Noble S. C., Gammie C. F., McKinney J. C., Del Zanna L., 2006, ApJ, 641, 626
Orszag S. A., Tang C. M., 1979, J. Fluid Mech., 90, 129
Owren B., Zennaro M., 1992, SIAM J. Sci. Stat. Comput., 13, 1488
Palenzuela C., Lehner L., Reula O., Rezzolla L., 2009, MNRAS, 394, 1727
Parés C., 2006, SIAM J. Numer. Anal., 44, 300
Persson P.-O., Peraire J., 2006, Proc. of the 44th AIAA Aerospace Sciences Meeting and Exhibit. AIAA-2006-112. Available at: https://doi.org/10.2514/6.2006-112
Peshkov I., Romenski E., 2016, Contin. Mech. Thermodyn., 28, 85
Porth O., Olivares H., Mizuno Y., Younsi Z., Rezzolla L., Moscibrodzka M., Falcke H., Kramer M., 2017, Comput. Astrophys. Cosmol., 4, 1
Puppo G., Semplice M., 2011, Commun. Comput. Phys., 10, 1132
Qiu J., Shu C., 2005, SIAM J. Sci. Comput., 26, 907
Qiu J., Shu C.-W., 2004, J. Comput. Phys., 193, 115
Qiu J., Dumbser M., Shu C., 2005, Comput. Methods Appl. Mech. Eng., 194, 4528
Radice D., Rezzolla L., 2011, Phys. Rev. D, 84, 024010
Radice D., Rezzolla L., 2012, A&A, 547, A26
Radice D., Rezzolla L., Galeazzi F., 2014, MNRAS Lett., 437, L46
Reed W., Hill T., 1973, Technical Report LA-UR-73-479, Triangular Mesh Methods for the Neutron Transport Equation. Los Alamos Scientific Laboratory
Rezzolla L., Zanotti O., 2013, Relativistic Hydrodynamics. Oxford Univ. Press, Oxford
Ritz W., 1909, J. Reine Angew. Math., 1909, 1
Rusanov V. V., 1961, J. Comput. Math. Phys. USSR, 1, 267
Semplice M., Coco A., Russo G., 2016, J. Sci. Comput., 66, 692
Shu C., 2016, J. Comput. Phys., 316, 598
Sonntag M., Munz C., 2014, in Fuhrmann J., Ohlberger M., Rohde C., eds, Finite Volumes for Complex Applications VII. Springer Int. Publ., Switzerland, p. 945
Sonntag M., Munz C., 2017, J. Sci. Comput., 70, 1262
Stroud A., 1971, Approximate Calculation of Multiple Integrals. Prentice-Hall Inc., Englewood Cliffs, NJ
Takahashi R., Umemura M., 2017, MNRAS, 464, 4567
Tavelli M., Dumbser M., 2016, J. Comput. Phys., 319, 294

Thorne K. S., Macdonald D., 1982, MNRAS, 198, 339
Titarev V. A., Toro E. F., 2002, J. Sci. Comput. 17, 609
Titarev V. A., Toro E. F., 2005, J. Comput. Phys., 204, 715
Toro E., 2009, Riemann Solvers and Numerical Methods for Fluid Dynamics, 3rd edn. Springer-Verlag, Berlin, Heidelberg
Toro E. F., Titarev V. A., 2006, J. Comput. Phys., 212, 150
Weinzierl T., Mehl M., 2011, SIAM J. Sci. Comput., 33, 2732
White C. J., Stone J. M., Gammie C. F., 2016, ApJS, 225, 22
Wilson J. R., 1975, Ann. New York Acad. Sci., 262, 123
York J. W., 1979, in Smarr L. L., ed., Sources of Gravitational Radiation. Cambridge Univ. Press, Cambridge, p. 83
Zhu J. Zhong X., Shu C.-W., Qiu J., 2013, J. Comp. Phys., 248, 200
Zanotti O., Dumbser M., 2015, Comput. Phys. Commun., 188, 110
Zanotti O., Dumbser M., 2016, Comput. Astrophys. Cosmol., 3, 1
Zanotti O., Fambri F., Dumbser M., Hidalgo A., 2015, Comput. Fluids, 118, 204
Zanotti O., Fambri F., Dumbser M., 2015, MNRAS, 452, 3010
Zhu J., Qiu J., Shu C.-W., Dumbser M., 2008, J. Comput. Phys., 227, 4330

APPENDIX A: TORUS INITIAL CONDITION

The acceleration experienced by a fluid element rotating around a compact object that acts as a source of gravity can be cast into the following differential equation:

$$\mathrm{d}\log|u_t| - \left(\frac{\Omega}{1-\Omega\ell}\right)\mathrm{d}\ell + \frac{\mathrm{d}p}{\rho h} = 0, \tag{A1}$$

where

$$\ell(r,\theta) := -\frac{u_\phi}{u_t}, \quad \Omega(r,\theta) := \frac{u^\phi}{u^t}, \tag{A2}$$

are the so-called specific angular momentum and the coordinate angular velocity, respectively. For barotropic fluids the last differential on the right in equation (A1) is exact, i.e. one can define the so-called effective potential $\mathcal{W}$ as

$$\mathcal{W} - \mathcal{W}_{\rm in} := -\int_0^p \frac{\mathrm{d}\tilde{p}}{\rho h} = \log|u_t| - \log|(u_t)|_{\rm in} - \int_{\ell_{\rm in}}^{\ell} \frac{\Omega \mathrm{d}\tilde{\ell}}{1-\Omega\tilde{\ell}}. \tag{A3}$$

In the test-case considered here, the specific angular momentum is assumed to be constant $\ell = \ell_0 = \text{const.}$, so that it is possible to obtain an explicit and simplified expression for the potential

$$\mathcal{W}(r,\theta) = \log|u_t|, \tag{A4}$$

where, for a Schwarzschild black hole, one has

$$u_t = -r\sin\theta\left(\frac{r-2}{r^3\sin^2\theta - \ell^2(r-2)}\right)^{\frac{1}{2}}. \tag{A5}$$

In the axisymmetric equilibrium torus, there are some special radial positions in the equatorial plane ($\theta = \pi/2$) that are worthwhile recalling: the inner and outer edges of the torus $r_{\rm in}$ and $r_{\rm out}$; the radial position of the cusp, $r_{\rm cusp}$; the radial position of the maximum pressure peak, $r_{\rm c}$, which is the centre of the torus; the radial positions of the so-called marginally stable and marginally bound orbit, $r_{\rm ms}$ and $r_{\rm mb}$. The position of the cusp $r_{\rm cusp}$ and the centre $r_{\rm c}$ can be identified as the local extrema of the effective potential, but also by the condition $\ell_K = \ell_0$, where ℓ_K is the Keplerian specific angular momentum that is given by $\ell_K^2(r) := Mr^3/(r-2M)^2$. Similarly, also $r_{\rm ms}$ and $r_{\rm mb}$ are identified by the conditions $\ell_K = \ell_{\rm ms}$ and $\ell_K = \ell_{\rm mb}$. For a Schwarzschild (non-rotating) black hole: $\ell_{\rm ms} = (3\sqrt{6}/2)M$ and $\ell_{\rm mb} = 4M$, so that the corresponding to the radial positions are $r_{\rm ms} = 6M$ and $r_{\rm mb} = 4M$. Finally, the inner and outer radial positions, $r_{\rm in}$ and $r_{\rm out}$, can be estimated by the condition $\Delta\mathcal{W} := \mathcal{W}_{\rm in} - \mathcal{W}_{\rm cusp} = 0$. Indeed, whenever $\Delta\mathcal{W} > 0$ the orbit of the corresponding fluid particle is open, whenever $(\mathcal{W}_{\rm c} - \mathcal{W}_{\rm in}) < \Delta\mathcal{W} < 0$ the orbits are closed. The spatial volume delimited by the widest closed equipotential surface of the torus, i.e. $\mathcal{W} = \mathcal{W}_{\rm cusp}$ is named as the 'Roche lobe' of the torus. Using these definitions, several constraints need to be satisfied: first, the cusp $r_{\rm cusp}$ must necessarily be located within $r_{\rm mb}$ and $r_{\rm ms}$, and the inner edge $r_{\rm in}$ can be located anywhere within $r_{\rm cusp}$ and $r_{\rm c}$. For isentropic fluids obeying the polytropic equation of state

$$p = K\rho^\Gamma, \tag{A6}$$

K being the polytropic constant, Γ the polytropic exponent, an analytical expression for the rest-mass density exists and takes the form

$$\rho(r,\theta) = \left[\frac{\Gamma-1}{K\Gamma}\left(\exp(\mathcal{W}_{\rm in} - \mathcal{W}(r,\theta)) - 1\right)\right]^{1/(\Gamma-1)}. \tag{A7}$$

After choosing the value of the polytropic constant K, polytropic exponent Γ, the specific angular momentum ℓ_0, and the potential gap $\Delta\mathcal{W}$, then the Keplerian points are estimated after ensuring the following scalar equalities: for the radial position of the cusp $r_{\rm cusp}$,

$$\ell_K(r) = \ell_0, \quad \text{with} \quad r_{\rm hor} < r < r_{\rm ms}, \tag{A8}$$

for the centre $r_{\rm c}$, $r_{\rm hor}$ being the radial position of the horizon,

$$\ell_K(r) = \ell_0, \quad \text{with} \quad r_{\rm ms} < r. \tag{A9}$$

Then, the corresponding potentials $\mathcal{W}_{\rm cusp}$ and $\mathcal{W}_{\rm c}$ are evaluated according to equation (A4). On the other hand, the effective potential at the inner edge $\mathcal{W}_{\rm in}$ is computed according to the prescribed potential gap $\Delta\mathcal{W}$ after estimating

$$(u_t)_{\rm in} = (u_t)_{\rm cusp}\, \mathrm{e}^{\Delta\mathcal{W}}. \tag{A10}$$

Then, since the fluid distribution is inside the Roche lobe, the inner and outer edge positions $r_{\rm in}$ and $r_{\rm out}$ are computed through the conditions

$$u_t(r) = (u_t)_{\rm in} \quad \text{with} \quad r_{\rm cusp} < r < r_{\rm c}, \tag{A11}$$

and

$$u_t(r) = (u_t)_{\rm in} \quad \text{with} \quad r_{\rm c} < r, \tag{A12}$$

respectively. The rest-mass density at the centre $\rho_{\rm c}$ is provided directly by the analytical solution (A7), and the corresponding pressure $p_{\rm c}$ through the polytropic equation of state (A6). Finally, for every spatial position (r, θ) within the torus, i.e. which fulfils the condition

$$r > r_{\rm in} \quad \text{and} \quad \mathcal{W} < \mathcal{W}_{\rm in}, \tag{A13}$$

the angular velocity $\Omega(r,\theta)$ is computed through the definition (A2), the rest-mass density ρ directly from (A7), the pressure p from the polytropic equation of state (A6), and the velocity is given by

$$(v^r, v^\theta, v^\phi) = \left(\frac{\beta^r}{\alpha}, 0, \frac{1}{\alpha}(\Omega + \beta^\phi)\right). \tag{A14}$$

This paper has been typeset from a TEX/LATEX file prepared by the author.